Title

mmWave Lens-Based MIMO System for Suppressing Small-Scale Fading and Shadowing

Journal

IEEE Transactions on Wireless Communications, 19(8)

ISSN

1536-1276

Authors

Almasi, Mojtaba Ahmadi
Amiri, Roohollah
Jafarkhani, Hamid
et al.

Publication Date

2020-08-01

DOI

10.1109/twc.2020.2991776

Peer reviewed

MmWave Lens-based MIMO System for Suppressing Small-scale Fading and Shadowing

Mojtaba Ahmadi Almasi, *Student Member, IEEE,* Roohollah Amiri, *Student Member, IEEE,* Hamid Jafarkhani, *Fellow, IEEE,* and Hani Mehrpouyan, *Member, IEEE*

***Abstract*—In this paper, we propose a generalized millimeter-Wave (mmWave) reconfigurable antenna multiple-input multiple-output (RA-MIMO) architecture that takes advantage of lens antennas. The considered antennas can generate multiple independent beams simultaneously using a single RF chain. This property, together with RA-MIMO, is used to combat small-scale fading and shadowing in mmWave bands. To this end, first, we derive a channel matrix for RA-MIMO. Then, we use rate-one space-time block codes (STBCs), together with phase-shifters at the receive reconfigurable antennas, to suppress the effect of small-scale fading. We consider two kinds of phase shifters: i) ideal which is error-free and ii) digital which adds quantization error. The goal of phase-shifters is to convert a complex-valued channel matrix into real-valued. Hence, it is possible to use rate-one STBCs for any dimension of RA-MIMO. We investigate diversity gain and derive an upper bound for symbol error rate in cases of ideal and digital phase-shifters. We show that RA-MIMO achieves the full-diversity gain with ideal phase-shifters and the full-diversity gain for digital phase-shifters when the number of quantization bits is higher than one. We investigate RA-MIMO in the presence of shadowing. Our analysis demonstrates that, by increasing the dimension of RA-MIMO, the outage probability decreases which means the effect of shadowing decreases. Numerical results verify our theoretical derivations.**

***Index Terms*—5G, lens-based reconfigurable antenna, millimeter-Wave, MIMO, shadowing, small-scale fading, STBC.**

I. Introduction

MILLIMETER-WAVE (mmWave) technology operating in the 30-300 GHz range is emerging as a promising solution for the fifth generation (5G) of wireless communication systems by supporting a larger user base and higher speed links [2]. The existence of a large communication bandwidth at mmWave frequencies will enable mmWave systems to support multi Gigabits/sec speeds. However, significant large-scale fading, i.e., path loss and shadowing, channel sparsity in multiple input multiple output (MIMO) systems, small-scale fading, as well as hardware limitations and costs are all major obstacles for the deployment of mmWave systems.

To combat the severe path loss at mmWave frequencies, researchers have proposed using antennas with substantial directional gains and line-of-sight (LoS) links [3]. Directivity can be achieved by using large number of antennas at transmitters and receivers. Therefore, thanks to the short wavelength at mmWave frequencies, massive MIMO is used to mitigate severe path loss [4]–[19]. Regarding this, three beamforming architectures have been proposed for mmWave systems with massive MIMO: i) *digital* [4]–[6], ii) *analog* [7]–[9], and iii) *hybrid* [10]–[20].

The *digital beamforming* approach provides great flexibility in shaping the transmitted beams. However, it requires one radio frequency (RF) chain per antenna [4]–[6]. This results in significant cost and complexity in mmWave massive MIMO systems. Further, digital beamforming may result in significant delay due to a large number of channel parameters that must be estimated [4]. As an alternative, *analog beamforming* applies phase-shifters to shape the output beam with only one RF chain for all antennas [7]–[9]. Although analog beamforming is energy efficient and cost effective, it can only provide one highly directional beam which does not address the high data rate required for outdoor 5G networks [4]. A promising beamforming approach for the mmWave MIMO architecture is based on a combination of analog and digital beamforming, i.e., *hybrid beamforming*. The hybrid architecture aims to use the advantages of digital and analog architectures. That is, at low signal-to-noise ratio (SNR), the hybrid architecture performs only beamforming to combat the path loss, and at high SNR, it aims to transfer high data by performing multiplexing [8]. Due to significance of hybrid beamforming, in what follows, we review the existing architectures.

To the best of the authors' knowledge, three types of hybrid beamforming architectures have been proposed so far which are i) hybrid beamforming with phase-shifters (Fig. 2.(a) in Section II) [10]–[13], ii) hybrid beamforming with spherical and planar lens antennas (Fig. 2.(b) in Section II) [14]–[18], [20], and iii) hybrid beamforming with reconfigurable[1] micro-electromechanical systems (MEMS) integrated antennas [19]. In the first architecture, each RF chain is connected to all the antennas via phase-shifters to generate highly directional beams [10], [11]. However, it is indeed complex due to huge number of phase-shifters. To reduce the complexity, the concept of sub-connected network has been introduced in [12]. In this architecture, each RF chain is connected to a sub-group of antennas, which reduces the complexity at the cost of

This project is supported in part by the NSF EARS grant award number 1642865, 1642536 and NASA ULI grant award number NNX17AJ94A. This work was presented in part at IEEE ICC 2018 [1].

M. A. Almasi, R. Amiri, and H. Mehrpouyan are with the Department of Electrical and Computer Engineering, Boise State University, Boise, ID 83725, USA (e-mail: {mojtabaahmadialm@u.boisestate.edu, roohollahamiri@u.boisestate.edu, hanimehrpouyan@boisestate.edu}). H. Jafarkhani is with Center for Pervasive Communications & Computing, UC Irvine, CA, USA. (e-mail: hamidj@uci.edu)

[1]In general, the reconfigurable antennas are designed to reconfigure their operational frequency [21], [22], polarization [23], and/or pattern (beam) [24], [25]. Throughout this paper, the beam reconfigurable antennas are considered.

reducing the directionality of the beams. Later, [13] proposed a phase-shifter selection design to further reduce the complexity.

The second methodology has a completely different structure, where several RF chains are connected to a *lens antenna array* via a switching network known as *beamspace* MIMO [14]. In this architecture, instead of phase-shifters, a spherical lens antenna is used to constructively change the phase of each path and generate directional beams. Hence, without using phase-shifters, the transceiver antenna can generate a few orthogonal beams to achieve multiplexing gain for better utilization of the bandwidth and to preserve low hardware complexity. In addition, several works have studied the lens antenna array in mmWave systems [15]–[18]. In [15], an electromagnetic (EM) planar lens is integrated with an antenna array. In the uplink transmission, the EM lens focuses the energy of the desired signal and rejects the interference. This leads to performance gain and lower signal processing complexity. Zeng *et al.* [16] then proposed a new lens antenna array MIMO system and demonstrated that the array response follows a sinc function. Next, an RF lens-embedded massive MIMO system is investigated in [17]. The fabricated lens operates at the 77-GHz band and is shown to support a high gain in the desired direction. The work in [18] studied a cost-effective mmWave lens antenna array system. The authors show that by exploiting the angle-dependent energy, together with the angular sparsity of the mmWave channels, the wireless system can achieve optimal capacity, i.e., the capacity achieved by digital beamforming, with only a few RF chains and low-complexity single-carrier transmission.

The third methodology offers reconfigurable MEMS integrated antennas for mmWave frequencies. The MEMS-based reconfigurable antennas have been widely studied in sub-6 GHz systems [26]–[29]. In [27], the diversity gain of traditional MIMO systems are improved through the application of reconfigurable antennas at the receiver and space-time block codes (STBCs). Subsequently, [28] extends the technique proposed in [27] to a system with reconfigurable antennas at both transmitter and receiver sides. Later, a coding scheme was proposed for these MIMO systems over frequency-selective fading channels in [29]. Due to high hardware complexity, costs, and propagation properties of mmWave channels, the designed systems in [27]–[29] are not viable for mmWave systems. Regarding these antennas, recently, a hybrid MEMS-based reconfigurable antenna system has been suggested for mmWave transmission in [19]. It is shown that the MEMS-based reconfigurable antennas achieve high throughput gains.

All aforementioned hybrid architectures aim to reduce the hardware complexity and costs, partially resolve the path loss issue through beamforming gain, and increase the spectral efficiency through multiplexing gain. Nevertheless, there are remaining essential issues related to large-scale fading, small-scale fading, and channel sparsity that must be addressed [2], [3]. The current mmWave systems only concentrate on transferring high data rate at high SNRs through multiplexing gain, i.e., steering a few directional beams, and mitigating path loss at low SNRs through beamforming, i.e., steering a highly directional and strong beam [4]–[19]. Thus, the current mmWave transmission relies on sending each data stream through one channel. In what follows, we address the deficiencies of the current mmWave transmission systems.

Point-to-Point transmission in mmWave dense networks is usually power-limited (or equally noise-limited) [30], [31]. Moreover, due to high path loss and blockage, LoS channels are available at a short distance and are susceptible to outage probability [30], [31]. On the other hand, because of small-scale fading and large-scale fading, NLoS channels suffer from signal attenuation and fast fluctuations [2], [32], [33]. As such, experimental channel measurements reveal that mmWave NLoS channels experience log-normal shadowing with zero mean and variances of 8.7 and 8 dB at 28 and 73 GHz [33], respectively. Thus, even at high SNRs, transmission via one NLoS channel is unreliable and susceptible to deep fading which leads to frequent outages. Notice that in this paper, shadowing is defined as large-scale fluctuations in the received signal which is due to the scatterers. Shadowing due to buildings, human body and mobile objects which is common in LoS channels is defined as blockage. The blockage can be severe and may result in the received signal power to be below the noise floor level [33], [34]. It is worth mentioning that one technique to mitigate the effect of shadowing is micro-diversity [35], [36]. In this technique, whenever the channel between a user and a base station (BS) is in deep shadowing, the user is served by another BS with a better channel to the user. This technique is utilized in both sub-6 GHz [37] and mmWave frequencies [34]–[36]. In mmWave, the fast-changing shadowing situation will require frequent hand-over between the BSs which imposes excessive overhead. More importantly, LoS channels may not be always available between the user and the neighboring BSs. For instance, in [36] it is shown that when a user is connected to one BS, in a network with the density of 10^3 BSs per km^2, the probability of having one LoS channel is 0.9 (< 1).

To tackle small-scale and shadowing issues in mmWave bands, one viable solution is achieving channel diversity gain which is the subject of this paper. Toward this goal, lens-based reconfigurable antennas are deployed to design a new mmWave MIMO system. Recall that traditional sub-6 GHz MIMO systems can exploit beamforming, multiplexing gain, and diversity gain [37]. The diversity gain is a well-known technique for overcoming small-scale fading. To resolve shadowing, we notice that, fortunately, each cluster (channel) in mmWave systems experiences random and independent shadowing [32]–[34], [38]. The randomness and independence of clusters can make the proposed reconfigurable antenna MIMO (RA-MIMO) suitable to overcome the impact of shadowing. To this end, recently, the idea of using a single composite right-left handed (CRLH) leaky-wave antenna (LWA) in a MIMO system instead of a massive antenna array was proposed in [39]. In this work, which is limited to just 2×2 MIMO systems, two reconfigurable LWAs are deployed at the transmitter in which each antenna steers several beams toward the receiver that is equipped with omni-directional antennas. Nevertheless, the recent designed lens antennas in [40] and [41] might represent better characteristics compared to that of LWAs that was considered in [39]. In this paper, inspired by [40] and [41], we propose an $N_t \times N_r$ lens-based RA-

MIMO architecture for mmWave communications. It is worth mentioning that mainly there are three differences between the proposed MIMO and hybrid beamforming with MEMS-based reconfigurable antennas. First, each lens-based reconfigurable antenna can steer multiple independent beams, while this unique property does not hold for MEMS-based reconfigurable antennas [41]–[43]. That is, the number of required RF chains in MEMS-based reconfigurable antennas is the same or greater than the number of data streams [19]. Second, in hybrid beamforming with MEMS-based reconfigurable antennas, all RF chain are connected to an antenna array [19], whereas in the proposed MIMO RF chains are separate and each RF chain is connected to a lens-based antenna. Third, the MEMS-based reconfigurable antennas can change the antenna's radiation pattern, polarization, and frequency [19], [26], [44]. However, in our paper, it is assumed that the lens-based antennas only reconfigure their radiation pattern. Although the proposed MIMO architecture can reconfigure radiation polarization and frequency by adequately designing the TSAs. Further, the proposed system aims to overcome small-scale and large-scale fading and keep the hardware complexity and costs low. The main contributions of this paper are:

1) A new lens-based MIMO architecture is proposed for point-to-point mmWave communications. Instead of using a large number of phase-shifters for beamforming, we use a lens antenna along with a switching network. Further, channel model that describes the relationship between the transmit and receiver signal is derived.
2) To improve reliability of mmWave links, we use rate-one STBCs. Our motivation to use STBCs is their advantage in reducing the error probability without requiring full channel state information (CSI) at the transmitter. The obtained diversity gain can mitigate small-scale fading and shadowing effects.
3) We evaluate the diversity gain and symbol error rate (SER) performance of the proposed system for ideal and digital phase-shifters assuming only small-scale fading. Further, an upper bound on SER is derived for the ideal and digital phase-shifters.
4) We evaluate outage probability when the impact of shadowing is included. The analysis reveals that RA-MIMO prevents deep shadowing through using several channels for the transmission.
5) Numerical simulations show that the proposed architecture outperforms hybrid beamforming systems in terms of diversity gain. Indeed, RA-MIMO with digital phase-shifters mostly achieves full-diversity at the cost of a slight coding gain loss. The impact of the number of transmit antennas on the received SNR and BER is presented.

The paper is organized as follows: Section II presents the channel model, the proposed RA-MIMO structure, and system parameters. Section III addresses small-scale fading by designing STBCs, evaluates full-diversity and error rate performance, and represents the system design tradeoffs. Section IV evaluates outage probability in presence of shadowing. In Section V, we present simulation results. Finally, Section VI concludes the paper.

Notations: Hereafter, $j = \sqrt{-1}$, small letters, bold letters and bold capital letters will designate scalars, vectors, and matrices, respectively. Superscript $(\cdot)^\dagger$ and $(\cdot)^*$ denote the transpose and transpose-conjugate operators, respectively. The sign $\angle(\cdot)$ stands for the phase of $(\cdot)$. $(\cdot)^{\text{Re}}$ and $(\cdot)^{\text{Im}}$ denote the real and imaginary parts of $(\cdot)$, respectively. $\mathbf{I}_n$ denotes the $n \times n$ identity matrix. Next, vec$(\cdot)$ denotes the vectorization of $\mathbf{A}$ which is a column vector obtained by stacking the columns of the matrix on top of one another. Further, $\mathbb{E}(\cdot)$, $|\cdot|$, and $||\cdot||^2$ denote the expected value, absolute value, and norm-2 of $(\cdot)$, respectively. $(\cdot)^{-1}$ and tr$(\cdot)$ denote the inverse and the trace of matrix $(\cdot)$, respectively. $Q(x)$ denotes the Q-function and is defined as $Q(x) = \frac{1}{\sqrt{2\pi}} \int_x^\infty \exp\left(-\frac{u^2}{2}\right) du$. Finally, $\mathbf{A} \circ \mathbf{B}$ and $\mathbf{A} \otimes \mathbf{B}$ stand for the Hadamard product and the Kronecker product of matrices $\mathbf{A}$ and $\mathbf{B}$, respectively.

II. The Proposed RA-MIMO Structure

A. Channel Model

1) MmWave propagation channel model: Due to the highly directional mmWave propagation, a typical mmWave channel contains only a few paths [33], [45]. Further, only one cluster contributes to each path. Thus, the number of clusters is the same as the number of paths [33], [45]. In general, a cluster channel model based on the extended Saleh-Valenzuela channel model has been widely adopted in mmWave communications [10]–[12], [14], [15], [19]. Regarding this model, the channel matrix $\mathbf{H}_0$ for a uniform planar array (UPA) is expressed by

$$\mathbf{H}_0 = \sum_{d=1}^{D} \mathbf{H}_d, \tag{1}$$

where D is the number of propagation paths, and $\mathbf{H}_d$ denotes the dth single path channel matrix given by

$$\mathbf{H}_d = \varpi_d \mathbf{a}_r(\phi^r_{\text{az},d}, \phi^r_{\text{el},d}) \mathbf{a}^*_t(\phi^t_{\text{az},d}, \phi^t_{\text{el},d}),$$

where $\varpi_d = \alpha_d \beta_d$ is the product of small-scale fading ($\alpha_a \in \mathbb{C}$) and large-scale fading ($\beta_d \in \mathbb{R}$) of the dth path. The parameters α_d and β_d will be discussed later in the rest of the paper. $\phi^r_{\text{az},d}$ ($\phi^r_{\text{el},d}$) and $\phi^t_{\text{az},d}$ ($\phi^t_{\text{el},d}$) are random azimuth (elevation) angle of arrival (AoA) and angle of departure (AoD), respectively. The vectors $\mathbf{a}_r$ and $\mathbf{a}_t$ represent the array response vectors at the corresponding AoA and AoD. Suppose the UPA is of dimension $N_x \times N_y$ in which N_x (N_y) denotes the number of elements of x-axis (y-axis). The array response vector $\mathbf{a}(\phi_{\text{az},d}, \phi_{\text{el},d})$ can be defined as

$$\mathbf{a}(\phi_{\text{az}}, \phi_{\text{el}}) = \frac{1}{\sqrt{N_x N_y}} \left[1, \ldots, e^{-j\pi\phi_{m,n}}, \ldots, e^{-j\pi\phi_{N_x-1,N_y-1}}\right]^\dagger, \tag{2}$$

where $\phi_{m,n} = \frac{2d'}{\lambda} \left(m \sin\phi_{\text{az},d} \cos\phi_{\text{el},d} + n \sin\phi_{\text{az},d} \sin\phi_{\text{el},d}\right)$ for $m \in \{0, \ldots, N_x - 1\}$ and $n \in \{0, \ldots, N_y - 1\}$. λ and d' are the wavelength and antenna spacing, respectively. Each path or cluster consists of $N_{\text{ray}} = N_x N_y$ rays.

In (1), D channels are considered in the considered mmWave propagation environment. It is worth mentioning that D represents the number of propagation paths established

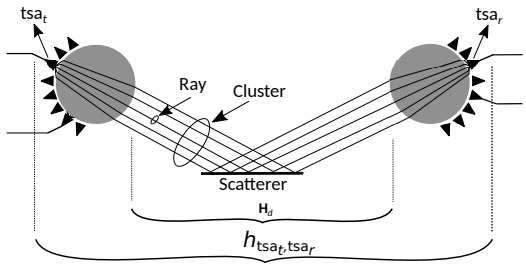

Fig. 1: Two different types of channel for a single path. The channel matrix $\mathbf{H}_d$ describes the dth channel between transmit lens antenna and receive lens antenna based on the cluster-based Saleh-Valenzuela model. h_{tsa_t,tsa_r} denotes the channel between TSA tsa$_t$ located on the transmit lens and TSA tsa$_r$ on the receive lens.

via NLoS channels which are due to scatterers between the transceiver. In practice, mmWave LoS channels exist in short distances and variation of the received signal due to small-scale fading and shadowing is negligible. In contrast to LoS channels, mmWave NLoS channels are impaired by small-scale and large-scale fading. Further, it is worth noting that the probability of having NLoS channels in mmWave frequencies, e.g., at 28 and 73 GHz, is much higher than LoS channels [33].

2) Channel model between a transceiver lens antenna pair: In what follows, we derive the channel model between two lens-based reconfigurable antennas. Before this, let us introduce a lens-based reconfigurable antenna. Each antenna contains four main functional blocks: i) **RF transceiver chain** which modulates and demodulates data signal. ii) **Beam selection network** is connected to the output of the RF chain and has multiple outputs that are connected to the input ports of the tapered slot antenna (TSA) feeds. iii) **TSA feeds** are located on the focal surface of a spherical lens. Each TSA feed steers a beam. iv) **A spherical lens** is positioned in front of the TSA feeds. Note that, for simplicity, hereafter, we use the terms TSA, lens, and lens antenna instead of TSA feeds, a spherical lens, and lens-based reconfigurable antenna, respectively. Further, N_{TSA} TSAs are located on the surface of each lens. The lens acts as a passive phase-shifter network. Each plane wave goes through the lens. After shifting the plane wave with different delays by the lens, the energy of the plane wave is focused on one of the focal points. When a plane wave hits the surface of a lens, the incident plane wave is focused on the antipodal point on the lens [46], [47]. Accordingly, when a feed antenna on the focal point sends a wave through the lens, a plane wave departs the lens as in Fig. 1. We now define each plane wave with the channel gain, direction information, and N_{ray} rays. Therefore, the model $\mathbf{H}_0$ is a suitable model to describe the channel between two lenses.

3) Channel model between a transceiver TSA pair: The channel impulse response for the dth path, i.e., $\mathbf{H}_d$ in Fig. 1, from a TSA at the transmit lens antenna, say tsa$_t$, to a TSA at the receive lens antenna, say tsa$_r$, is obtained as [16]

$$h_{\text{tsa}_t,\text{tsa}_r} = \varpi_d \sqrt{A_t A_r}, \tag{3}$$

for tsa$_t$ $= 1, 2, \ldots, N_{\text{TSA}}$ and tsa$_r$ $= 1, 2, \ldots, N_{\text{TSA}}$, where A_t and A_r denote respectively the transmit and receive lens aperture size. Here, A_t and A_r are directly related to N_{ray}, such that a bigger aperture means more rays arrive or depart a lens. Further, ϖ_d for $d = 1, 2, \ldots, D$ is defined in (1). The remaining $D-1$ channel impulse responses can be defined in the same fashion.

B. The Proposed RA-MIMO Architecture

As discussed earlier, hybrid beamforming systems compensate the high path loss through beamforming. However, they are not able to suppress the effect of small-scale fading and specially shadowing in NLoS channels. To obtain reliable transmission links, this paper aims to propose a new mmWave MIMO structure. The proposed RA-MIMO is presented in Fig. 2. (c). Further, for comparison purposes, two well-known hybrid beamforming architectures are shown in Fig 2.(a) and (b). The proposed architecture has a fundamental property. In RA-MIMO, RF chains are separated and each of them is connected to a specific lens whereas those of the hybrid systems shown in Fig. 2.(a) and (b) are spaced closely and connected to the same antenna array and lens, respectively. Therefore, our RA-MIMO architecture provides the degree of freedom that ensures the number of MIMO channel paths is dictated by the number of antennas and not by the mmWave channel.

C. System Parameters

We assume an outdoor[2] frequency flat fading[3] mmWave transceiver system composed of RA-MIMO at both the transmitter and the receiver as shown in Fig. 2.(c). Further, it is assumed that the transceiver is located in an urban area where a large number of scattering objects are available. Therefore, sufficient independent paths are established. The transmitter and the receiver are equipped with N_t and N_r lens antennas, respectively. It is worth mentioning that each transmit reconfigure antenna steers N_r beams. Analogously, each receiver reconfigure antenna steers N_t beams.

1) Channel matrix: To determine the channel matrix of RA-MIMO, we notice that according to Fig. 2(c) there is only one channel between each transceiver lens antenna pair. That is, the n_tth antenna totally generates N_r beams, one beam for each receiver antenna. Analogously, the n_rth receive antenna totally generates N_t beams, one beam for each transmit antenna. It should be emphasized that according to (1), D channels are established between each transceiver lens antenna pair. However, only one of the existing D channels is selected between each transceiver lens antenna pair. Therefore, (3) describes the channel at the TSA's outputs of a transceiver lens antenna pair. The channel between the n_tth lens antenna and the n_rth lens antenna at the TSA's outputs, by changing

[2]For indoor communications in mmWave bands, analog systems are considered in which the transmitter and receiver are equipped with on RF chain [7]–[9]. In this case, transmission is done through one beam. Our proposed system can be used in indoor communications as well if only one RF chain and one beam are assumed.

[3]In the case of frequency selective fading, certain modulation schemes such as orthogonal frequency division multiplexing (OFDM) can be directly deployed in the proposed RA-MIMO to provide robustness to the fading.

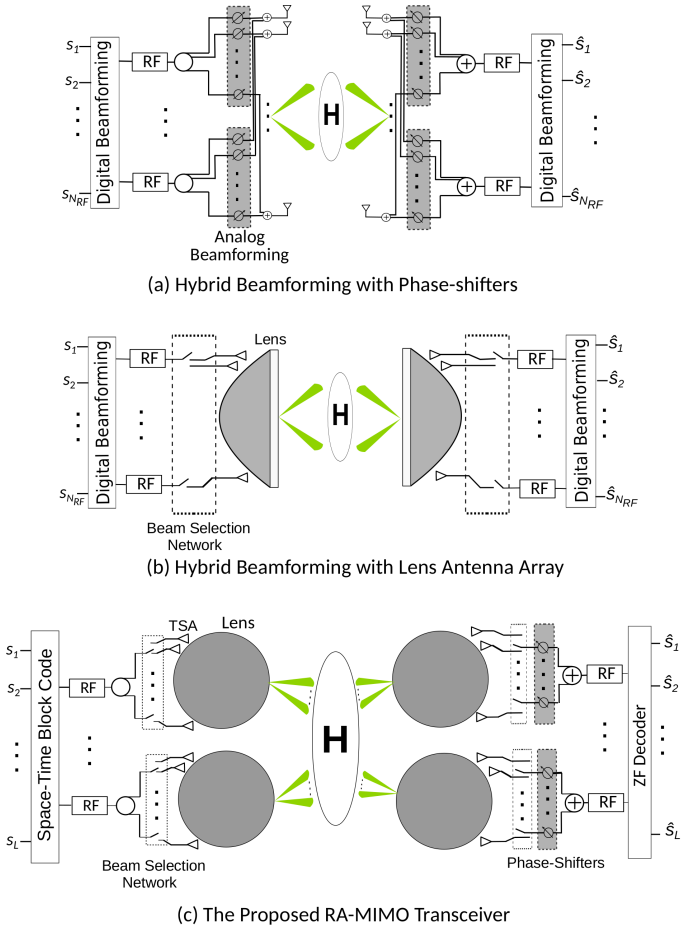

Fig. 2: Three different mmWave architectures: (a) Hybrid beamforming with RF chains and phase-shifters [10]; (b) Hybrid beamforming with lens antenna array [14]; (c) The proposed RA-MIMO transceiver based on lens antennas. It is assumed that all channels are NLoS.

the notations of (3), becomes h_{n_t,n_r}. Eventually, the channel matrix $\mathbf{H}$ is expressed as

$$\mathbf{H} = [h_{n_t,n_r}]_{N_t \times N_r}. \tag{4}$$

It is important to note that in order to make sure $\mathbf{H}$ is full-rank, each channel should be used by only one transceiver pair. Hence, we have $N_t N_r \leq D$. In this paper, it is assumed that the number of scattering objects (D) is sufficiently high. In the case that the number of scatterers is not high enough, the performance of RA-MIMO might be limited. One viable solution is that the antennas should be sufficiently separated such that multiple independent channels can be established by using one scatterer.

2) Reconfigured channel matrix: As outlined in [41], the proposed lens antenna can simultaneously change the phase of each beam. That is to say, in a single transmit/receive lens antenna, each TSA would be equipped by a phase-shifter and can change the phase of its signal independently. Although, we assume that only the receive lens antennas are equipped by phase-shifters. This is because in a mmWave MIMO system, the CSI associated to small-scale fading varies rapidly compared to the direction of each beam [48]. Since the steering direction changes slowly, this information can be useful at the transmitter. However, the fast varying CSI is of little value at the transmitter by the time it is estimated at the receiver and fed back. In our design, we assume that there is no CSI available at the transmitter. However, AoD and AoA information are respectively available at the transmitter. Mathematically, we represent role of the phase-shifters with matrix $\mathbf{G} = [g_{n_t,n_r}]_{N_t \times N_r}$. This matrix is called reconfigurable parameter matrix of lens antenna. The parameter g_{n_t,n_r} is related to the n_tth beam of the n_rth antenna and is determined as

$$g_{n_t,n_r} = e^{j\theta_{n_t,n_r}},\ n_t = 1,2,\ldots,N_t,\ n_r = 1,2,\ldots,N_r, \tag{5}$$

where θ_{n_t,n_r} denotes the phase of the corresponding phase-shifter at the receiver.

To realize the connection between the channel matrix and the reconfigurable parameter matrices, assume that a typical information signal, s, is sent from the n_rth beam of the n_tth antenna. The signal is then multiplied by the channel coefficient between the n_tth and the n_rth antenna, i.e., $s \times h_{n_t,n_r}$. At the receiver, it is multiplied by g_{n_t,n_r}. That is, the received signal is equal to $s \times h_{n_t,n_r} g_{n_t,n_r}$ without considering the noise term. This expression indicates that there is a one-to-one mapping among the entries of $\mathbf{G}$ and $\mathbf{H}$ at the receiver side. Hence, the Hadamard product can nicely describe this mapping. That is, the reconfigurability brings about a new matrix denoted by reconfigured channel matrix or $\mathbf{H}_g$, where

$$\mathbf{H}_g = \mathbf{H} \circ \mathbf{G}. \tag{6}$$

$\mathbf{H}_g = (\mathbf{h}_{g,1}, \mathbf{h}_{g,2}, \ldots, \mathbf{h}_{g,N_r})$ of size $N_t \times N_r$ with entries $\mathbf{h}_{g,n_r}$ of size $N_t \times 1$. Here, $\mathbf{h}_{g,n_r}$ denotes the reconfigured channel between the transmitter and the n_rth receiver antenna.

3) Signal and noise model: Now, we express the relationship between the transmit and receive antennas in baseband as

$$\mathbf{Y} = \sqrt{\frac{P_t}{N_t N_r}} \mathbf{X}(\mathbf{s}) \mathbf{H}_g + \mathbf{Z}, \tag{7}$$

where $\mathbf{Y} = (\mathbf{y}_1, \mathbf{y}_2, \ldots, \mathbf{y}_{N_r})$ is the $T \times N_r$ received signal matrix. P_t denotes the transmit power. The factor $\frac{P_t}{N_t N_r}$ is per beam transmit power. More details about this factor will be provided in Section III-C. T is the number of time slots in each block. $\mathbf{X}(\mathbf{s})$ is a $T \times N_t$ STBC matrix and $\mathbf{s} = (s_1, s_2, \ldots, s_L)^\dagger$ is the $L \times 1$ information signal vector, where its elements are drawn from constellation $\mathcal{A}$. $\mathbf{H}_g$ of size $N_t \times N_r$ is defined in (6). The elements of the $T \times N_r$ noise matrix, $\mathbf{Z} = (\mathbf{z}_1, \mathbf{z}_2, \ldots, \mathbf{z}_{N_r})$, are modeled by independent identically distributed (i.i.d) complex Gaussian random variables with zero mean and σ^2 variance, i.e., $z_{t,n_r} \sim \mathcal{CN} = (0, \sigma^2)$, where $\sigma = \sqrt{\mathbb{E}\{|z_{t,n_r}|^2\}}$ for $t = 1,2,\ldots,T$ and $n_r = 1,2,\ldots,N_r$. The value of σ depends on the number of selected beams at each receive antennas. Compared to the traditional MIMO systems, (7) contains the reconfigured channel matrix ($\mathbf{H}_g$) rather than the channel matrix ($\mathbf{H}$). The parameters $\mathbf{G}$ and $\mathbf{X}(\mathbf{s})$ in (7) are flexible and should be designed.

It is worth mentioning that channel estimation is one of the important issues in implementing RA-MIMO. We divide channel estimation into two steps. At the first step, using beam

search algorithms, the direction information (AoD and AoA) of each path is determined. Then, the small-scale fading and the large-scale fading are estimated. Since we assume that the lens antennas are sufficiently close, all D scatters between a typical transceiver can be seen by all antennas. This means if the channel between one transmit and one receiver antenna is estimated, the estimation is valid for all transceiver pairs. Due to the directional transmission, finding accurate direction information is not trivial. Two main direction estimation algorithms in the mmWave band are i) exhaustive beam search [49] and ii) hierarchical beam search [50]. Both algorithms are extensively studied in hybrid beamforming systems with phase-shifters and are directly or indirectly applicable in RA-MIMO system.

Beam selection is another important issue for RA-MIMO. A proper beam selection method can increase diversity gain. Although, in this paper, our focus is on diversity gain obtained from STBCs and phase-shifters. To this end, only $D = N_r N_t$ channels are consider to be available and each transceiver pair selects a channel randomly. Notice that all channels are estimated before. Further, it is assumed that the channels experience the same path loss. This assumption is almost firm since the channels are considered to be NLoS [33]. However, in the case that number of channels is higher than $N_t N_r$ and each channel experiences different path loss, beam selection combined with STBCs can increase the diversity gain. That is, as $D > N_t N_r$, some or all transceiver antenna pairs have more than one option to select beam. So, an efficient beam selection algorithm will definitely lead to higher diversity gain. Some of the initial results on beam selection can be found in [51]. Channel estimation and beam selection are subject of future research.

In what follows, we analyse the performance of the proposed RA-MIMO considering the effect of small-scale fading and large-scale fading. The probability density function (PDF) of the small-scale fading and large-scale fading when they are superimposed is highly complicated [52, Eq. (6)]. Therefore, the analysis of the joint impact of small-scale fading and shadow fading will be intractable. Although a simplified expression for the PDF is studied, the obtained PDF is still complicated [53, Eq. (3)] and the analysis will not be easy to follow. Hence, due to the complicated PDF, the small-scale fading and large-scale fading are evaluated separately.

III. Overcoming Small-Scale Fading

Each element of channel matrix $\mathbf{H}$ contains the effect of small-scale, large-scale fading and the transceiver lens gain. In this section, only small-scale fading is assumed and the effect of large-scale fading and the transceiver lens gain are dealt with in the next section. Hence, we assume $h_{n_r,n_t} = \alpha_d$, and small-scale fading is modeled by Rayleigh fading, i.e., $\alpha_d \sim \mathcal{CN}(0,\,1)$[4]. The importance of suppressing the impact of small-scale fading is that the rapid and high fluctuations of the channel can cause unreliable handover decisions and transmission link failures [54].

[4]In this paper, to provide insight to the impact of the proposed system on the performance of mmWave NLoS channels, Rayleigh fading is assumed. The case of Nakagami fading which generalizes Rayleigh fading and approximates Rician fading is subject of the future work.

A. Design of System Parameters

1) Design of θ_{n_t,n_r}: When the signal is received from multiple paths, the best technique to enhance the received SNR is to use maximum ratio combining (MRC) [55]. Utilizing the MRC technique requires weighing the signals proportional to the inverse of the channel coefficient amplitudes before combining. However, due to using phase-shifters in the RA-MIMO, this technique is not practical.

The alternative technique to improve the received SNR is the equal gain combining (EGC) [55]. This technique equally weights and co-phases the signals. Therefore, we have

$$\theta_{n_t,n_r} = -\angle h_{n_t,n_r}, \quad n_t = 1,2,\ldots,N_t,\; n_r = 1,2,\ldots,N_r. \tag{8}$$

Thus, $g_{n_t,n_r} = e^{-j\angle h_{n_t,n_r}}$, and $\mathbf{H}_g$ in (6) is a non-negative real-valued matrix while the channel matrix, $\mathbf{H}$, is complex-valued. In this section, we consider ideal phase-shifters, while digital phase-shifters are covered in Section III-B. It is worth mentioning that in the case of wide-band transmission, a single value of a phase shift will not be valid across the whole band. To overcome this issue, one feasible solution is to deploy filter bank behind TSAs [56]. Next, phase of a received signal at the output of each filter is changed by using a phase-shifter. Then, the output signals are combined.

2) Design of the STBC Matrix $\mathbf{X}(\mathbf{s})$: To attain full-diversity gain when CSI is not available at the transmitter, space-time block coding is considered as a promising method. STBCs have been designed for both real and complex channels [37]. Real STBCs are used for transmission over real-valued channels, and the complex STBCs are utilized for transmission over complex-valued channels. Note that the channel matrix, $\mathbf{H}$, in our system is complex-valued and naturally a complex STBC can be used. However, we propose compensating for the channel phase, as done in (8), and using a real STBC. Since real-valued rate-one orthogonal STBCs (OSTBCs) that provide the maximum diversity and simple symbol-by-symbol decoding exist for any number of transmit antennas, this will allow us to utilize a rate-one STBC and reduce the overall complexity by using linear receivers such as ZF. **Note that rate-one complex OSTBCs do no exist for more than two antennas [57].**

A set of real-valued square STBCs for $N_t = 2, 4$, and 8 have been designed in [57]. These STBCs are suitable candidates for the proposed RA-MIMO even though here we use them with complex constellation points. Two examples of rate-one $\mathbf{X}(\mathbf{s})$ for $N_t = 2$ and 4 are given by [57] as

$$\mathbf{X}(\mathbf{s}) = \begin{bmatrix} s_1 & s_2 \\ -s_2 & s_1 \end{bmatrix}, \tag{9}$$

and

$$\mathbf{X}(\mathbf{s}) = \begin{bmatrix} s_1 & s_2 & s_3 & s_4 \\ -s_2 & s_1 & -s_4 & s_3 \\ -s_3 & s_4 & s_1 & -s_2 \\ -s_4 & -s_3 & s_2 & s_1 \end{bmatrix}, \tag{10}$$

respectively. Note that while the codes are similar to the STBC in ([57], Eqs. (3) and (4)), their application in the proposed

design is different. Other codes for any number of antennas can be found in [57]. All these codes can be represented as

$$\mathbf{X}(\mathbf{s}) = \mathbf{A}_1 s_1 + \mathbf{A}_2 s_2 + \cdots + \mathbf{A}_L s_L, \tag{11}$$

where $\mathbf{A}_\ell$ of size $T \times N_t$ is Hurwitz-Radon family of matrices which its entries are restricted to the set $\{-1,0,1\}$. In our design, the information symbols s_ℓ for $\ell = 1, 2, \ldots, L$ in (11) are drawn from a complex-valued constellation. Further, in [57], it is proved that these matrices have the following properties:

$$\begin{aligned} \mathbf{A}_k^\dagger \mathbf{A}_k &= \mathbf{I}_{N_t}, && k = 1,2,\ldots,L, \\ \mathbf{A}_k^\dagger \mathbf{A}_\ell &= -\mathbf{A}_\ell \mathbf{A}_k^\dagger, && 1 \le k < \ell \le L. \end{aligned} \tag{12}$$

The most important observation about (12) is that for $\ell = k$ the matrices are orthogonal and for $\ell \neq k$ they are skew-symmetric. In what follows, we will use these properties to evaluate the STBCs in our RA-MIMO system.

Remark 1. As mentioned, there is a specific difference between the STBCs in [57] and the ones in this paper. The STBC defined by (11) encodes **complex-valued symbols**, whereas [57] encodes **real-valued symbols**. Nevertheless, in both cases, the code rate is equal to one, and the codes facilitate low complexity decoding.

Remark 2. To encode complex-valued information symbols for $N_t = 2$ and 4, the OSTBC [58] and the Quasi-OSTBC (QOSTBC) [59] are well-suited rate-one codes. However, those codes are designed for a complex-valued channel matrix in which s and the conjugate of s are encoded to achieve full-diversity gain. Although the channel matrix $\mathbf{H}$ in our system is complex-valued, thanks to the lens antennas and phase compensation in (8), the complex-valued elements are converted into real-valued. That is, the reconfigure channel matrix in (6) is real-valued. Therefore, the conjugate of the information symbols is not required.

Remark 3. While real OSTBCs exist for any number of antennas, for more than four antennas, low complexity rate-one full-diversity complex STBCs are not available [57]. As such, in addition to low complexity and full-diversity, the rate advantage of the proposed system will result in a high coding gain for a large number of transmit antennas.

B. Diversity and Error Probability Evaluation

This section studies the achievable diversity gain and derives an upper bound for error probability in the presence of digital phase-shifters. The limited resolution of digital phase-shifters can affect the performance of the proposed RA-MIMO system regarding diversity and coding gain. Full-diversity is the most important factor in designing STBCs because it dramatically reduces the error probability. On the other hand, coding gain is important since at high SNR regions a low coding gain can cause a big difference in error probability. Therefore, we first study the full-diversity and SER performance of the utilized STBCs with ideal phase-shifters. Then, we perform full-diversity and SER analysis for the digital phase-shifters.

1) Ideal phase-shifter: By ideal phase-shifter, we mean the phase-shifters have unlimited resolution and (8) holds. The following lemma demonstrates that under ideal phase-shifter the proposed RA-MIMO system achieves full-diversity.

Lemma 1. The proposed RA-MIMO system achieves full-diversity with linear receivers and ideal phase-shifters.

Proof. See Appendix A. □

Accordingly, the upper bound expression for the SER is given in the following theorem.

Theorem 1. In RA-MIMO system, the upper bound of the SER when using a ZF receiver with the cardinality of M is obtained as

$$\mathrm{P}(\hat{s}_\ell \to s_\ell) \le \frac{M-1}{M} a^{-N_t N_r} \rho^{-N_t N_r}, \tag{13}$$

where $a = \frac{3}{2(M^2-1)}, \frac{\sin^2(\pi/M)}{2}$, and $\frac{3}{4(M-1)}$ for PAM, PSK, and square QAM constellations, respectively. Also, ρ denotes the average received SNR of each symbol which is given by

$$\rho_\ell = \frac{P_t}{N_t N_r} \frac{1}{\left(\boldsymbol{\mathcal{S}}^{-1}\right)_{\ell,\ell} \sigma^2} = \frac{P_t}{N_t N_r} \frac{\|\mathbf{h}_g\|^2}{\sigma^2}, \quad \ell = 1,\ 2,\ \cdots,\ L, \tag{14}$$

where $\boldsymbol{\mathcal{S}}$ is defined in (22) and the second equality follows from (22) in Appendix A.

Proof. See Theorem 1 in [60]. □

Theorem 1 reveals that the upper bound is not affected by the reconfigured channel matrix. This means the proposed RA-MIMO reaches the maximum coding gain with the ZF receiver, which is usually sub-optimal for other systems. Consequently, minimum mean square error (MMSE) attains the maximum coding gain as well as a maximum likelihood (ML) receiver.

2) Digital phase-shifter: In real-time applications, limited resolution of digital phase-shifters becomes a serious challenge for achieving full-diversity gain. The reason is that the discrete resolution of the phase-shifter does not allow it to completely compensate the phase of channel coefficients. When B-bit resolution phase-shifters are employed, the options to select a proper phase are constrained to be $\{0, \ldots, (2^B - 1)2\pi/2^B\}$. Therefore, the reconfigured channel matrix $\mathbf{H}_g$ given by (6) is no longer real. This would diminish the diversity gain and coding gain.

Lemma 2. For any number of encoded symbols L, the proposed RA-MIMO system can achieve full-diversity with a linear receiver and a B-bit resolution digital phase-shifter for $B > 1$. While providing full-diversity, small values of B may result in an ill-conditioned system.

Proof. See Appendix B. □

Theorem 2. The upper bound of the SER of RA-MIMO system using B-bit digital phase-shifters for $B = 2$ is given by

$$\mathrm{P}(\hat{s}_\ell \to s_\ell) < \frac{M-1}{M} a^{-N_t N_r} \rho^{-N_t N_r} C'^{-N_t N_r}, \tag{15}$$

where $C' = \frac{1}{C}\left(\frac{L}{L-1}\right)^{L-1}$ in which C is given by $\det(\bar{\bar{\boldsymbol{\mathcal{S}}}}^{-1}) \geq C$ and $\bar{\bar{\boldsymbol{\mathcal{S}}}}$ denotes the normalization of (24) presented in Appendix B.

Proof. See Appendix C. □

C. System Design Tradeoffs

In sub-6 GHz MIMO systems which are equipped with omni-directional antennas, the power is divided per antennas. As said in Section II, the power in RA-MIMO is divided per beam. It is because in RA-MIMO each beam is steered by a single TSA. Since each TSA is an independent antenna, at the transmitter, power is divided by the number of all beams, i.e., $N_t N_r$. On the other hand, at the receiver, each independent TSA adds an $i.i.d$ noise term to its own received signal. For instance, in a receive lens antenna with b beams, the received signal contains b $i.i.d$ noise terms. This is not true in sub-6 GHz MIMO systems. That is, in sub-6 GHz MIMO systems, a signal received through an omni-directional antenna, directional antennas, or reconfigurable antennas which add only one AWGN noise to the received signal. Since the number of beams of each lens antenna equals to the number of transmit lens antennas (N_t), increasing N_t will likely impose more noise terms which reduces the received SNR. This issue is shown by the following corollary.

Corollary 1. In RA-MIMO system, the average received SNR is given by

$$\rho = \frac{P_t}{N_t \sigma_n^2}, \tag{16}$$

where σ_n^2 is variance of the noise at each TSA.

Proof. See Appendix D. □

Remark 4. Although it seems that the value of N_r can affect the received SNR (See Eq. (7)), Corollary 1 indicates that only N_t has impact on the received SNR. This important finding leads to a tradeoff in designing RA-MIMO systems. That is, for various N_t, the proposed RA-MIMO will show different received SNR, which can lead to different coding gains. For instance, suppose two RA-MIMO systems achieve the same diversity gain with different number of transmit and receive antennas, i.e., $N_t N_r = N_t' N_r'$. It is obvious that, for $N_t > N_t'$, we will have $N_r < N_r'$. Using (16), the second system attains a higher coding gain since it has less number of antennas compared to the first system.

IV. Overcoming Shadowing

Large-scale fading contains two parts, path loss denoted by $\Upsilon^{-\frac{n}{2}}$ and shadowing denoted by β_d, e.g., $\beta_d' = \Upsilon^{-\frac{n}{2}}\beta_d$, where Υ is the distance between the transmitter and receiver, n is the path loss factor. More precisely, path loss is defined as the constant reduction at the received SNR as the distance between the transmitter and the receiver increases. The path loss factor highly depends on the propagation environment and the operational frequency. The values of the factor for different environments and operational frequencies at mmWave bands are obtained in [33]. Two common ways of overcoming path loss are increasing the transmit power and the transceiver antenna gain. It is stated that the energy focusing property of the lens acts like beamforming [47] which increases the received SNR by $\sqrt{A_t A_r}$ gain. Hence, it is supposed that the path loss is made up by the transmit power and the lenses. Therefore, we normalize the channel coefficient (3) by $\Upsilon^{-\frac{n}{2}}\sqrt{A_t A_r}$ which results in $h_{n_r,n_t} = \alpha_d \beta_d$. In what follows, we only concentrate on the impact of shadowing.

To focus on the impact of shadowing, we assume the impact of amplitude of small-scale fading is averaged out, i.e., $|\alpha_d| = 1$, and only consider the channel phase and shadowing, i.e., $h_{n_r,n_t} = e^{j\angle\alpha_d}\beta_d$. The obtained channel gain after applying (8), i.e., passing through the ideal phase-shifter, becomes $h_{g,n_r,n_t} = \beta_d$. Studies indicate that β_d^2 has a log-normal distribution with parameters μ and η^2 [33]. Applying logarithm operator on β_d^2 leads to a simple representation of shadowing such that $10\log_{10}\beta_d^2 \sim \mathcal{N}(\mu,\, \eta^2)$ in which $\mu = 0$ and η depends on the environment and operating frequency [33]. In the case of huge fluctuations, outage probability is supposed to be a proper criterion to evaluate performance of a system [33]. It should be noticed that the analysis is conducted for the ideal phase-shifters. The impact of using digital phase-shifters on the performance of RA-MIMO in the presence of shadowing is eliminated due to space limitations.

Theorem 3. The approximated outage probability for the proposed RA-MIMO under the influence of shadowing is given by

$$p_{\text{out}} \approx 1 - Q\left(\frac{10\log_{10}\left(\frac{\gamma\sigma^2 N_t N_r}{P_t}\right) - \mu'}{\eta'}\right), \tag{17}$$

where γ is the predefined threshold for outage probability. Also, μ' and η'^2 denote the mean and variance of the random variable $10\log_{10}\left(\|\mathbf{h}_g\|^2\right)$ which approximately has a normal distribution.

Proof. See Appendix E. □

Remark 5. One cannot use traditional MIMO systems with omni-directional antennas and STBCs in mmWave bands due to high path loss. Hence, RA-MIMO provides an ability to benefit from traditional MIMO structures by using more directional gain antennas to both overcome path loss and shadowing and small-scale fading based on the proposed methodology. Further, one alternative may be using only one RF chain combined with equal gain combining. This causes feedback overhead and using high-speed switches and phase-shifters since the best beam should frequently be selected at the transmitter and receiver. Feedback overhead reduces the allocated time for data transmission and high-speed switches and phase-shifters operating as mmWave frequencies are extremely expensive. Moreover, in this paper we aim to overcome both the small-scale fading and the large-scale fading. To this end, we have proposed a MIMO architecture in which several replicas of a transmit signal are received. This enables the proposed MIMO system to simultaneously overcome the small-scale fading and the large-scale fading. However, in a system with one RF chain

and equal gain combining it is impossible to simultaneously overcome the small-scale fading and large-scale fading.

Remark 6. The proposed RA-MIMO can be used in point-to-point wireless communications such as backhaul, fronthaul, and access links as well as in multi-user scenarios [42], [43]. Moreover, it can be used for mmWave communications in presence of LoS and NLoS channels. Especially, in LoS channels, the channel matrix becomes ill-conditioned and by adjusting the distance between the lenses which depends on the distance between the transmitter and receiver, a full-rank channel is obtained [61]. Further, transmit and receive diversity techniques as well as multiplexing techniques can be used in conjunction with RA-MIMO system. RA-MIMO has a flexible structure which means the number of RF chains at the transmitter can be different from the receiver. Whereas, the existing hybrid beamforming systems require the same number of RF chains at transmitter and receiver ends. [4]–[19]. That is to say, in hybrid beamforming systems, multiple data streams are sent simultaneously. Each data stream requires one RF chain at transmitter and one RF chain at receiver. Hence, the number of RF chains at transmitter and receiver should be the same. Last but not least, the lens antenna separation leads to the use of common scatterers to establish mutually orthogonal channels and therefore to achieve higher diversity gain or multiplexing gain [62].

V. Numerical Results

This section presents the numerical simulations for the proposed RA-MIMO in Fig. 2(c) along with the STBCs in (11) and ZF receivers. The communication channel is modeled as a Rayleigh fading channel where the channel parameters are modeled by a zero-mean and unit-variance Gaussian distribution. For shadowing, we consider an outdoor environment in an urban area, where the shadowing parameters are modeled by a log-normal distribution with a zero-mean and variance of 8 dB for each channel as modeled in [33]. Next, we note that there are three different types of hybrid beamforming systems mentioned in Section I. As such, these hybrid beamforming systems provide different beamforming gains that result in different throughputs. In particular, each hybrid beamforming transceiver has a beamforming gain, say G_t at transmitter or G_r at receiver. In the simulations, we set $G_t = G_r = 1$. That is, before the normalization, the received SNR is given by $\frac{P_t G_t G_r |h|^2}{N_t \sigma_n^2}$, where P_t and $|h|^2$ denote the transmit power and the channel gain, respectively, and σ_n^2 denotes the noise power. Further, due to a fixed distance between the transmitter and the receiver, the effect of pathloss is fixed and neglected. After normalization of the SNR by the beamforming gain $G_t G_r$, the same SNR is obtained for all three hybrid systems which is given by $\frac{P_t |h|^2}{N_t \sigma_n^2}$. On the other hand, our goal is to compare the proposed RA-MIMO with the hybrid beamforming systems in terms of the diversity gain. Since beamforming gain does not affect the diversity gain, it is rational to consider a normalized SNR. Hence, far from which hybrid beamforming system is considered for comparison, diversity gain is always the same. Throughout the simulations the term hybrid beamforming includes all the three types. Moreover, the STBCs in (9) and (10) are exploited in the hybrid beamforming systems for diversity gain comparison. Further, the described channel conditions for the RA-MIMO are also used for the scenario of hybrid beamforming. To make a fair comparison, we normalize the SNR of RA-MIMO system with its beamforming gain as well.

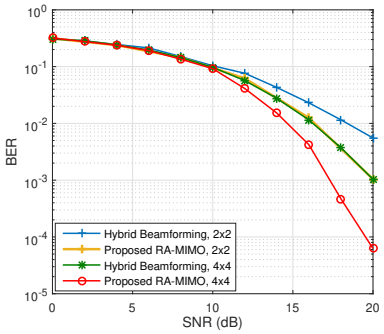

Fig. 3: BER performance of the hybrid beamforming system and the proposed RA-MIMO of size 2×2 and 4×4.

A. BER Performance Comparison

Fig. 3 shows the BER performance of the hybrid beamforming and the proposed RA-MIMO systems versus SNR for a throughput of 4 bits/s/Hz. For a 2×2 MIMO system, the symbols are drawn from 16-QAM and encoded by (9). The results show that RA-MIMO achieves diversity of order 4, i.e., full-diversity gain, whereas, the hybrid beamforming system shows a diversity of order 2 since each transmitted signal is sent through one path at each time slot. Further, BER comparison is plotted for RA-MIMO and hybrid beamforming systems for a 4×4 MIMO. The symbols are encoded via (10). Likewise, the proposed RA-MIMO achieves diversity gain 16, i.e., full-diversity, while the hybrid beamforming gives diversity of order 4. Hence, the BER is remarkably reduced. That is to say, transmission via the RA-MIMO is more reliable than the hybrid beamforming. Another important result is that the proposed RA-MIMO system can achieve same diversity gain as the hybrid beamforming system using less RF chains. For instance, for a diversity of order 4, the hybrid beamforming system requires 4 RF chains, while the RA-MIMO needs 2 RF chains. In general, maximum diversity gain that can be achieved by the hybrid beamforming system is N_{RF}, where N_{RF} denotes number of RF chains. Whereas, the proposed RA-MIMO needs only $\lceil \sqrt{N_{\text{RF}}} \rceil$ RF chains to achieve same or more diversity gain, where $\lceil . \rceil$ denotes the ceiling function.

B. BER Performance of Digital Phase-shifters

Fig. 4 shows BER curves for the RA-MIMO of dimension 2×2 with digital phase-shifters with $B = 1, 2, 3,$ and 4. In this simulation, the STBC in (9) is used to encode two symbols ($L = 2$) over two time slots ($T = 2$). For comparison, the ideal phase-shifters are also considered. For $B = 1$, RA-MIMO does not provide full-diversity gain as shown in Appendix B. Simulation indicates that RA-MIMO achieves the full-diversity gain for the resolution of digital phase-shifters greater than 1 as well as ideal phase-shifters. This is consistent

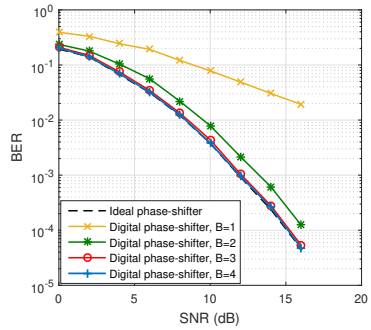

Fig. 4: BER performance of 2×2 RA-MIMO versus SNR with ideal and digital phase-shifters.

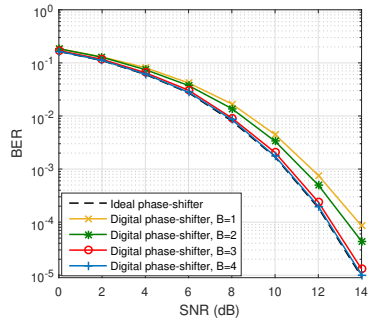

Fig. 5: BER performance of 4×4 RA-MIMO versus SNR with ideal and digital phase-shifters.

with Lemma 2 and Theorem 2. Further, as expected for low resolutions like ($B = 2$), RA-MIMO loses about 1 dB coding gain at BER=10^{-4} compared to that of the ideal phase-shifters. However, by increasing the number of bits in digital phase-shifters, the BER performance approaches to that of ideal phase-shifters such that for $B = 3$ and 4 the performances are approximately the same. The reason for a lower coding gain compared to the ideal phase-shifters is that in the case of digital phase-shifters due to the quatization error, the off-diagonal elements of the channel matrix in (24) are not zero. Thus, the channel's eigenvalues may not be equal as discussed in Theorem 2 which leads to a lower coding gain.

To show more comparison, we simulate RA-MIMO of dimension 4×4 by assuming the STBC in (10). Fig. 5 depicts the BER curves versus SNR of various resolutions for the digital phase-shifters. RA-MIMO with the ideal phase-shifters achieves full-diversity gain. However, as expected, the digital phase-shifters with $B = 2$, 3, and 4 achieve full-diversity gain, whereas, for $B = 1$, RA-MIMO does not provide full-diversity. It is worth noting that in the case of $B = 2$, the reconfigured channel becomes ill-conditioned as mentioned in Appendix B. This would severely degrade the coding gain of the system. Further, for $B = 3$ and 4, RA-MIMO with digital phase-shifters approximately attains the same coding gain as that of ideal phase-shifters.

C. System Design Tradeoff

Fig. 6 reveals the impact of the antenna configuration on the BER performance of RA-MIMO. As it is mentioned in

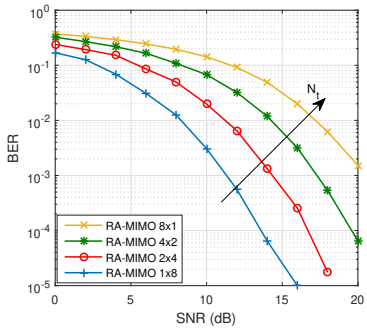

Fig. 6: BER performance for different antenna configurations.

Section III-C, N_t scales the received SNR such that increasing the N_t diminishes the SNR. To investigate this, we assume 4 different RA-MIMO antenna configurations 8×1, 4×2, 2×4, and 1×8. The last RA-MIMO uses a single-input multiple-output structure (SIMO) which is a special case of RA-MIMO. From Fig. 6 we conclude that all 4 RA-MIMO configurations achieve full-diversity gain but different coding gains. This verifies Corollary 1.

D. Outage Probability

In Fig. 7, the outage probability performance is illustrated for a hybrid beamforming system with two RF chains and different dimensions of RA-MIMO system. For the hybrid beamforming system, it is assumed that the transceiver is equipped with two RF chains, and two streams are simultaneously sent over two NLoS channels shown by "Hybrid Beamforming 2×2". For RA-MIMO, three configurations 2×2, 2×3, and 2×4 are considered. The threshold γ is set to 0 dB. As shown, the hybrid beamforming system provides the highest outage probability which is the worst performance. That is, using only one NLoS channel for transmission of a data stream will bring up frequent fluctuations which increases outage probability. Whereas, RA-MIMO is able to reduce outage probability when more number of NLoS channels are utilized. At SNR 40 dB, outage probability for the hybrid beamforming system is about 10^{-1}, while that of RA-MIMO for 2×2, 2×3, and 2×4 are 10^{-2}, 10^{-3}, and 10^{-5}, respectively. In addition, the derived expression for outage probability in Theorem 3 is also plotted. The simulation indicates that when the exact PDF of random variable v is replaced by an approximated normal distribution, the obtained outage probability is accurately fitted to the actual value of outage probability. By doing exhaustive search over various values, the log-normal parameters μ' and η' are obtained as follows. For RA-MIMO of dimensions 2×2, 2×3, and 2×4, the values of μ' are respectively given as 15, 16.9, and 17.9 and those of η' are respectively obtained as 9.7, 7.8, and 6.7 dB. Further, the parameters of the hybrid beamforming system is obtained as $\mu' = 8$ and $\eta' = 13$. It is revealed that by increasing the dimension of RA-MIMO μ' rises and η' diminishes.

VI. Conclusion

In this paper, a RA-MIMO system for mmWave wireless communications is proposed. RA-MIMO is inspired from the

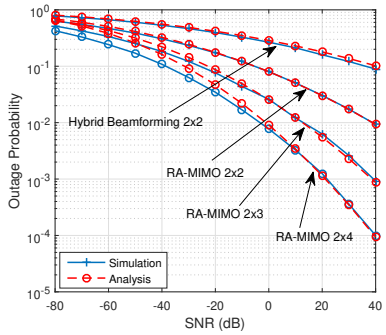

Fig. 7: Comparison of outage probability between a hybrid beamforming system and various RA-MIMO configurations.

lens antennas and its aim is to combat small-scale fading and shadowing at mmWave frequencies. First of all, the channel matrix for the RA-MIMO is derived. Then, by using the lens antennas along with ideal phase-shifters, the complex-valued channel matrix is converted to the real-valued one. Further, RA-MIMO achieves full-diversity when complex-valued STBCs are utilized. Next, studying a practical scenario, it is shown that even with the digital phase-shifters, the system achieves full-diversity when the phase-shifters' resolution is greater than one-bit at the cost of losing coding gain. Upper bounds are derived for the SER performance in both ideal and digital phase-shifters. By calculating the received SNR with respect to N_t, a tradeoff between the number of transmit antennas and coding gain is found. Lastly, the outage probability of RA-MIMO in the presence of shadowing is studied. The numerical results confirm our analytical findings.

Appendix A
Proof of Lemma 1

By plugging (11) into (7), the received signal can be rewritten as

$$\begin{aligned}\mathbf{Y} &= \sqrt{\frac{P_t}{N_t N_r}}\left(\mathbf{A}_1 s_1 + \mathbf{A}_2 s_2 + \cdots + \mathbf{A}_L s_L\right)\mathbf{H}_g + \mathbf{Z} \\ &= \sqrt{\frac{P_t}{N_t N_r}}\left(\mathbf{A}_1 \mathbf{H}_g s_1 + \mathbf{A}_2 \mathbf{H}_g s_2 + \cdots + \mathbf{A}_L \mathbf{H}_g s_L\right) + \mathbf{Z}.\end{aligned} \tag{18}$$

Defining $\mathbf{h}_g = \text{vec}(\mathbf{H}_g)$, $\mathbf{g} = \text{vec}(\mathbf{G})$, and $\mathbf{h} = \text{vec}(\mathbf{H})$, we define $\mathbf{b}_\ell$ as $\mathbf{b}_\ell = (\mathbf{I}_{N_r} \otimes \mathbf{A}_\ell)\,\mathbf{h}_g \triangleq (\mathbf{I}_{N_r} \otimes \mathbf{A}_\ell)\,(\mathbf{h} \circ \mathbf{g})$ for $\ell = 1, \ldots, L$. Then, vectorization of (18) results in

$$\bar{\mathbf{y}} = \sqrt{\frac{P_t}{N_t N_r}}\left[\mathbf{b}_1, \mathbf{b}_2, \ldots, \mathbf{b}_L\right]\mathbf{s} + \bar{\mathbf{z}}, \tag{19}$$

where $\bar{\mathbf{y}} = \text{vec}(\mathbf{Y})$ and $\bar{\mathbf{z}} = \text{vec}(\mathbf{Z})$ are $TN_r \times 1$ vectors. Also, we define $\boldsymbol{\mathcal{H}}_g = \left(\mathbf{b}_1, \mathbf{b}_2, \ldots, \mathbf{b}_L\right)$ as the equivalent reconfigured channel matrix. $\boldsymbol{\mathcal{H}}_g$ is a real-valued matrix since $\mathbf{h} \circ \mathbf{g}$ represents the real vector $\mathbf{h}_g$ with entries equal to the amplitude of the channel coefficients. Matrix $\boldsymbol{\mathcal{H}}_g$ matrix exists when $\mathbf{H}_g$ is non-zero. Thus, (19) can be rewritten as $\bar{\mathbf{y}} = \sqrt{\frac{P_t}{N_t N_r}}\boldsymbol{\mathcal{H}}_g \mathbf{s} + \bar{\mathbf{z}}$. After applying the ZF receiver, the estimated $\hat{\mathbf{s}}_{\text{ZF}}$ is given by

$$\begin{aligned}\hat{\mathbf{s}}_{\text{ZF}} &= \sqrt{\frac{N_t N_r}{P_t}}\left(\boldsymbol{\mathcal{H}}_g^\dagger \boldsymbol{\mathcal{H}}_g\right)^{-1}\boldsymbol{\mathcal{H}}_g^\dagger \bar{\mathbf{y}} \\ &= \mathbf{s} + \sqrt{\frac{N_t N_r}{P_t}}\left(\boldsymbol{\mathcal{H}}_g^\dagger \boldsymbol{\mathcal{H}}_g\right)^{-1}\boldsymbol{\mathcal{H}}_g^\dagger \bar{\mathbf{z}}.\end{aligned} \tag{20}$$

The existence of (20) depends on the existence of $\left(\boldsymbol{\mathcal{H}}_g^\dagger \boldsymbol{\mathcal{H}}_g\right)^{-1}$. Hence, $\boldsymbol{\mathcal{H}}_g^\dagger \boldsymbol{\mathcal{H}}_g$ should be full-rank. It is shown in [63] that for any real-valued $n \times 1$ vector $\mathbf{v}$, we have

$$\mathbf{v}^\dagger \mathbf{A}_k^\dagger \mathbf{A}_\ell \mathbf{v} = \delta_{kl}\mathbf{v}^\dagger \mathbf{v},\ k, \ell = 1, \ldots, L, \tag{21}$$

where $\delta_{k,l}$ is the Kronecker delta function and is 1 when $k = l$ and 0 when $k \neq l$. Considering that $\boldsymbol{\mathcal{H}}_g$ is real-valued and referring to (21), we can derive that

$$\boldsymbol{\mathcal{S}} \triangleq \boldsymbol{\mathcal{H}}_g^\dagger \boldsymbol{\mathcal{H}}_g \triangleq \|\mathbf{h}_g\|^2 \mathbf{I}_L. \tag{22}$$

Consequently, we have $\det(\boldsymbol{\mathcal{S}}) = \|\mathbf{h}_g\|^{2L}$, which is always non-zero. Eq. (22) indicates that the equivalent reconfigured channel matrix is orthogonal, which means the linear receivers achieve full-diversity gain [60] for the STBC defined in (11) under ideal phase-shifters.

Appendix B
Proof of Lemma 2

In the case of digital phase-shifters, the equivalent reconfigured channel matrix is expressed as $\tilde{\boldsymbol{\mathcal{H}}}_g = \left[\tilde{\mathbf{b}}_1, \ldots, \tilde{\mathbf{b}}_L\right]$, where $\tilde{\mathbf{b}}_\ell$ is given by $\tilde{\mathbf{b}}_\ell = (\mathbf{I}_{N_r} \otimes \mathbf{A}_\ell)\,\tilde{\mathbf{h}}_g \triangleq (\mathbf{I}_{N_r} \otimes \mathbf{A}_\ell)\,(\tilde{\mathbf{g}} \circ \mathbf{h})$ for $\ell = 1, \ldots, L$, with $\tilde{\mathbf{g}} = \text{vec}(\tilde{\mathbf{G}})$. The matrix $\tilde{\mathbf{G}}$ represents the receive lens antenna parameter for digital phase-shifters. The elements of $\tilde{\mathbf{G}}$ are defined as $\tilde{g}_{n_t,n_r} = e^{-j\tilde{\theta}_{n_t,n_r}}$. The quantized phase $\tilde{\theta}_{n_t,n_r}$ is obtained as

$$\begin{aligned}\tilde{\theta}_{n_t,n_r} =& \arg \min_{\theta_{n_t,n_r}} |\angle h_{n_t,n_r} - \theta_{n_t,n_r}|, \\ &\text{subject to } \theta_{n_t,n_r} \in \{0, \ldots, \frac{(2^B - 1)2\pi}{2^B}\}.\end{aligned} \tag{23}$$

Since digital phase-shifters are not able to provide the exact value of the channel's phase, the vector $\tilde{\mathbf{b}}_\ell$ is not real-valued. It is simple to show that $\tilde{\mathbf{b}}_\ell^* \tilde{\mathbf{b}}_k \neq 0$, for $\ell \neq k$. Thus, the matrix $\tilde{\boldsymbol{\mathcal{H}}}_g^* \tilde{\boldsymbol{\mathcal{H}}}_g$ is not orthogonal. This would cast doubt on the existence of the ZF matrix in (20) when digital phase-shifters are employed. In order to study (20), we obtain $\boldsymbol{\mathcal{S}}$ in the case of digital phase shifting, $\tilde{\boldsymbol{\mathcal{S}}}$, as

$$\tilde{\boldsymbol{\mathcal{S}}} \triangleq \tilde{\boldsymbol{\mathcal{H}}}_g^* \tilde{\boldsymbol{\mathcal{H}}}_g = \begin{bmatrix} \|\mathbf{h}_g\|^2 & \tilde{\mathbf{b}}_1^* \tilde{\mathbf{b}}_2 & \cdots & \tilde{\mathbf{b}}_1^* \tilde{\mathbf{b}}_L \\ \tilde{\mathbf{b}}_2^* \tilde{\mathbf{b}}_1 & \|\mathbf{h}_g\|^2 & \cdots & \tilde{\mathbf{b}}_2^* \tilde{\mathbf{b}}_L \\ \vdots & \vdots & \ddots & \vdots \\ \tilde{\mathbf{b}}_L^* \tilde{\mathbf{b}}_1 & \tilde{\mathbf{b}}_L^* \tilde{\mathbf{b}}_2 & \cdots & \|\mathbf{h}_g\|^2 \end{bmatrix}. \tag{24}$$

Each off-diagonal element in $\tilde{\boldsymbol{\mathcal{S}}}$ is given by

$$\begin{aligned}\tilde{\mathbf{b}}_k^* \tilde{\mathbf{b}}_\ell = \tilde{\mathbf{h}}_g^* \mathbf{A}_k^\dagger \mathbf{A}_\ell \tilde{\mathbf{h}}_g &= \left(\tilde{\mathbf{h}}_g^{\text{Re}\dagger} - j\tilde{\mathbf{h}}_g^{\text{Im}\dagger}\right)\mathbf{A}_k^\dagger \mathbf{A}_\ell \left(\tilde{\mathbf{h}}_g^{\text{Re}} + j\tilde{\mathbf{h}}_g^{\text{Im}}\right) \\ &\overset{(a)}{=} j\tilde{\mathbf{h}}_g^{\text{Re}\dagger} \mathbf{A}_k^\dagger \mathbf{A}_\ell \tilde{\mathbf{h}}_g^{\text{Im}} - j\tilde{\mathbf{h}}_g^{\text{Im}\dagger} \mathbf{A}_k^\dagger \mathbf{A}_\ell \tilde{\mathbf{h}}_g^{\text{Re}} \\ &\overset{(b)}{=} 2j\tilde{\mathbf{h}}_g^{\text{Re}\dagger} \mathbf{A}_k^\dagger \mathbf{A}_\ell \tilde{\mathbf{h}}_g^{\text{Im}}.\end{aligned} \tag{25}$$

To obtain (a), for $\ell \neq k$, we notice that based on (21) we have $\tilde{\mathbf{h}}_g^{\text{Re}\dagger}\mathbf{A}_k^\dagger\mathbf{A}_\ell\tilde{\mathbf{h}}_g^{\text{Re}} = 0$ and $\tilde{\mathbf{h}}_g^{\text{Im}\dagger}\mathbf{A}_k^\dagger\mathbf{A}_\ell\tilde{\mathbf{h}}_g^{\text{Im}} = 0$. For Step (b), we rewrite the second term of (a) as $j\tilde{\mathbf{h}}_g^{\text{Im}\dagger}\mathbf{A}_\ell^\dagger\mathbf{A}_k\tilde{\mathbf{h}}_g^{\text{Re}}$. Noting that $\tilde{\mathbf{h}}_g^{\text{Im}\dagger}\mathbf{A}_\ell^\dagger\mathbf{A}_k\tilde{\mathbf{h}}_g^{\text{Re}}$ is a scalar real value, after applying the transpose operation, it can be rewritten as $\tilde{\mathbf{h}}_g^{\text{Re}\dagger}\mathbf{A}_k^\dagger\mathbf{A}_\ell\tilde{\mathbf{h}}_g^{\text{Im}}$. Thus, the two terms in (a) are the same and (b) is valid.

To continue from (25), we consider the property of the Hurwitz-Radon family of matrices where each column and row only contains one non-zero element which is either 1 or -1. In [57], it is revealed that $\mathbf{A}_k^\dagger\mathbf{A}_\ell$ is also the Hurwitz-Radon set of matrices, which means $\mathbf{A}_k^\dagger\mathbf{A}_\ell$ is skew-symmetric. Let (m,n) for $m,n = 1,2,\ldots,L$ denote the position of the non-zero element of the mth row and the nth column in matrix $\mathbf{A}_k^\dagger\mathbf{A}_\ell$. Since the matrix is skew-symmetric, for any non-zero element at (m,n), the element (n,m) is non-zero and its value is negative of the value of the element (m,n). Further, let vector $\mathbf{i}_{k,\ell}^1$ contain the first elements of all (m,n) pairs and vector $\mathbf{i}_{k,\ell}^2$ contain the second elements of all (m,n) pairs. For instance, let $\mathbf{A}_k^\dagger\mathbf{A}_\ell = [0\ 1\ 0\ 0; -1\ 0\ 0\ 0; 0\ 0\ 0\ -1; 0\ 0\ 1\ 0]$. In this 4×4 matrix, the non-zero elements are positioned in $(2,1)$, $(1,2)$, $(4,3)$, and $(3,4)$ which yields $\mathbf{i}_{k,\ell}^1 = (2,1,4,3)$ and $\mathbf{i}_{k,\ell}^2 = (1,2,3,4)$. Hence, it is not hard to see that for $k \neq \ell$

$$\begin{aligned}\tilde{\mathbf{b}}_k^*\tilde{\mathbf{b}}_\ell &= 2j\textstyle\sum_{q=1}^{L}(-1)^{q+1}h^{\text{Re}}_{g,\mathbf{i}^1_{k,\ell}(q)}h^{\text{Im}}_{g,\mathbf{i}^2_{k,\ell}(q)}\\ &\overset{(c)}{=} 2j\textstyle\sum_{q=1}^{L/2}\Big(h^{\text{Re}}_{g,\mathbf{i}^1_{k,\ell}(2q-1)}h^{\text{Im}}_{g,\mathbf{i}^2_{k,\ell}(2q-1)} - \\ &\qquad\qquad h^{\text{Re}}_{g,\mathbf{i}^1_{k,\ell}(2q)}h^{\text{Im}}_{g,\mathbf{i}^2_{k,\ell}(2q)}\Big)\\ &\overset{(d)}{=} -2j\textstyle\sum_{q=1}^{L/2}h_{g,\mathbf{i}^1_{k,\ell}(2q-1)}h_{g,\mathbf{i}^2_{k,\ell}(2q-1)}\sin\left(\Delta\delta_{k,\ell}\right).\end{aligned} \tag{26}$$

Step (c) follows from the skew-symmetric property of $\mathbf{A}_k^\dagger\mathbf{A}_\ell$ which is shown in (12). To get (d), we replace $h^{\text{Re}}_{g,\mathbf{i}^1_{k,\ell}(2q-1)}$ and $h^{\text{Im}}_{g,\mathbf{i}^2_{k,\ell}(2q-1)}$ by $h_{g,\mathbf{i}^1_{k,\ell}(2q-1)}\cos(\delta_{\mathbf{i}^1_{k,\ell}(2q-1)})$ and $h_{g,\mathbf{i}^2_{k,\ell}(2q-1)}\sin(\delta_{\mathbf{i}^2_{k,\ell}(2q-1)})$, respectively, in which δ denotes the difference between the phase of the channel coefficient and the phase-shifter, then notice that $\sin x\cos y - \cos x\sin y = \sin(x-y)$. Also, we define $\Delta\delta_{k,\ell} = \delta_{\mathbf{i}^1_{k,\ell}(2q-1)} - \delta_{\mathbf{i}^2_{k,\ell}(2q-1)}$. The maximum absolute value of $\tilde{\mathbf{b}}_k^*\tilde{\mathbf{b}}_\ell$ is obtained when $\Delta\delta_{k,\ell} = 2\pi/2^{B+1}$. To take the resolution of the phase-shifters into account, we define a new matrix $\hat{\boldsymbol{\mathcal{S}}}$ where the off-diagonal elements are denoted by $\hat{\mathbf{b}}_k^*\hat{\mathbf{b}}_\ell$. For $\Delta\delta_{k,\ell} = \frac{2\pi}{2^{B+1}}$, the absolute value of each off-diagonal element is defined as

$$\left|\hat{\mathbf{b}}_k^*\hat{\mathbf{b}}_\ell\right| = 2\sin\left(\frac{2\pi}{2^{B+1}}\right)\textstyle\sum_{q=1}^{L/2}h_{g,\mathbf{i}^1_{k,\ell}(2q-1)}h_{g,\mathbf{i}^2_{k,\ell}(2q-1)}. \tag{27}$$

We notice that each off-diagonal element is either $\hat{\mathbf{b}}_k^*\hat{\mathbf{b}}_\ell = j\left|\hat{\mathbf{b}}_k^*\hat{\mathbf{b}}_\ell\right|$ or $\hat{\mathbf{b}}_k^*\hat{\mathbf{b}}_\ell = -j\left|\hat{\mathbf{b}}_k^*\hat{\mathbf{b}}_\ell\right|$. The diagonal elements are equal to $\tilde{\mathbf{b}}_\ell^*\tilde{\mathbf{b}}_\ell \triangleq \hat{\mathbf{b}}_\ell^*\hat{\mathbf{b}}_\ell = \|\mathbf{h}_g\|^2$. In what follows, we aim to find an upper bound for the off-diagonal elements of $\hat{\boldsymbol{\mathcal{S}}}$ which will be justified below. For a fixed phase-shifter resolution, the entries of $\hat{\boldsymbol{\mathcal{S}}}$ vary only with respect to the amplitude of the channel coefficients. Hence, we can normalize the amplitude of channel and rewrite $\hat{\boldsymbol{\mathcal{S}}}$ as $\hat{\boldsymbol{\mathcal{S}}} \triangleq \|\mathbf{h}_g\|^2\bar{\bar{\boldsymbol{\mathcal{S}}}}$ in which the diagonal elements of $\bar{\bar{\boldsymbol{\mathcal{S}}}}$ are equal to 1 and absolute value of the upper bound of off-diagonal elements are given by

$$\begin{aligned}\left|\bar{\bar{\mathbf{b}}}_k^*\bar{\bar{\mathbf{b}}}_\ell\right| &= \sin\left(\frac{2\pi}{2^{B+1}}\right)\frac{2\sum_{q=1}^{L/2}h_{g,\mathbf{i}^1_{k,\ell}(2q-1)}h_{g,\mathbf{i}^2_{k,\ell}(2q-1)}}{\|\mathbf{h}_g\|^2}\\ &\leq \sin\left(\frac{2\pi}{2^{B+1}}\right).\end{aligned} \tag{28}$$

The inequality is due to $\frac{2\sum_{q=1}^{L/2}h_{g,\mathbf{i}^1_{k,\ell}(2q-1)}h_{g,\mathbf{i}^2_{k,\ell}(2q-1)}}{\|\mathbf{h}_g\|^2} \leq 1$. To justify this, without loss of generality, we notice that for two arbitrary real scalars x and y the inequality $x^2+y^2 \geq 2xy$ always holds.

The matrix $\bar{\bar{\boldsymbol{\mathcal{S}}}}$ is positive definite if $\text{Re}\left(\boldsymbol{\upsilon}^*\bar{\bar{\boldsymbol{\mathcal{S}}}}\boldsymbol{\upsilon}\right) > 0$ holds for all non-zero vectors $\boldsymbol{\upsilon} \in \mathbb{C}^{L\times 1}$ [64]. Hence, we have

$$\begin{aligned}\boldsymbol{\upsilon}^*\bar{\bar{\boldsymbol{\mathcal{S}}}}\boldsymbol{\upsilon} &= \sum_{i=1}^{L}|\upsilon_i|^2 + \sum_{k=2}^{L}\sum_{\ell=1}^{k-1}\bar{\bar{\mathbf{b}}}_k^*\bar{\bar{\mathbf{b}}}_\ell\left(\upsilon_\ell{\upsilon_k}^* - {\upsilon_\ell}^*\upsilon_k\right)\\ &\overset{(a)}{=} \sum_{i=1}^{L}|\upsilon_i|^2 - 2\sum_{k=2}^{L}\sum_{\ell=1}^{k-1}\left(\bar{\bar{\mathbf{b}}}_k^*\bar{\bar{\mathbf{b}}}_\ell\right)^{\text{Im}}\left({\upsilon_\ell}^{\text{Im}}{\upsilon_k}^{\text{Re}} - {\upsilon_\ell}^{\text{Re}}{\upsilon_k}^{\text{Im}}\right)\\ &\overset{(b)}{=} \sum_{i=1}^{L}|\upsilon_i|^2 - 2\sum_{k=2}^{L}\sum_{\ell=1}^{k-1}\left(\bar{\bar{\mathbf{b}}}_k^*\bar{\bar{\mathbf{b}}}_\ell\right)^{\text{Im}}|\upsilon_k||\upsilon_\ell|\sin(\theta_\ell-\theta_k)\\ &\overset{(c)}{\geq} \sum_{i=1}^{L}|\upsilon_i|^2 - 2\sum_{k=2}^{L}\sum_{\ell=1}^{k-1}\left|\bar{\bar{\mathbf{b}}}_k^*\bar{\bar{\mathbf{b}}}_\ell\right||\upsilon_k||\upsilon_\ell|\\ &\overset{(d)}{\geq} \sum_{i=1}^{L}|\upsilon_i|^2 - 2\sin\left(\frac{2\pi}{2^{B+1}}\right)\sum_{k=2}^{L}\sum_{\ell=1}^{k-1}|\upsilon_k||\upsilon_\ell|\\ &\triangleq \boldsymbol{\upsilon}_{\text{abs}}^\dagger\bar{\bar{\boldsymbol{\mathcal{S}}}}_{\text{upper}}\boldsymbol{\upsilon}_{\text{abs}},\end{aligned} \tag{29}$$

where $\boldsymbol{\upsilon}_{\text{abs}}$ denotes the element-wise absolute value of $\boldsymbol{\upsilon}$ and $\bar{\bar{\boldsymbol{\mathcal{S}}}}_{\text{upper}}$ is obtained by replacing the off-diagonal elements of $\bar{\bar{\boldsymbol{\mathcal{S}}}}$ by the upper bound in (28). From (a), since the terms $\bar{\bar{\mathbf{b}}}_k^*\bar{\bar{\mathbf{b}}}_\ell$ and $\upsilon_\ell{\upsilon_k}^* - {\upsilon_\ell}^*\upsilon_k$ are purely imaginary, we get that $\boldsymbol{\upsilon}^*\bar{\bar{\boldsymbol{\mathcal{S}}}}\boldsymbol{\upsilon}$ is always real. For Step (b), we use ${\upsilon_\ell}^{\text{Re}} = |\upsilon_\ell|\cos\theta_\ell$ and ${\upsilon_\ell}^{\text{Im}} = |\upsilon_\ell|\sin\theta_\ell$ and $\sin\theta_\ell\cos\theta_k - \cos\theta_\ell\sin\theta_k = \sin(\theta_\ell-\theta_k)$. To obtain (c), we use the inequality $\left(\bar{\bar{\mathbf{b}}}_k^*\bar{\bar{\mathbf{b}}}_\ell\right)^{\text{Im}}\sin(\theta_\ell-\theta_k) \leq \left|\bar{\bar{\mathbf{b}}}_k^*\bar{\bar{\mathbf{b}}}_\ell\right|$. Then, replacing $\left|\bar{\bar{\mathbf{b}}}_k^*\bar{\bar{\mathbf{b}}}_\ell\right|$ by its maximum value $\left|\bar{\bar{\mathbf{b}}}_k^*\bar{\bar{\mathbf{b}}}_\ell\right|$ and using the upper bound $\left|\bar{\bar{\mathbf{b}}}_k^*\bar{\bar{\mathbf{b}}}_\ell\right| \leq \sin\left(\frac{2\pi}{2^{B+1}}\right)$ defined in (28) give (d).

Ineq. (29) reveals that instead of the complicated matrix $\bar{\bar{\boldsymbol{\mathcal{S}}}}$, we can evaluate the positive definite property of $\bar{\bar{\boldsymbol{\mathcal{S}}}}_{\text{upper}}$, i.e., if $\bar{\bar{\boldsymbol{\mathcal{S}}}}_{\text{upper}}$ is positive definite, $\bar{\bar{\boldsymbol{\mathcal{S}}}}_{\text{upper}}$ is positive definite as well. Note that the opposite is not true: $\bar{\bar{\boldsymbol{\mathcal{S}}}}_{\text{upper}}$ may not be full-rank while $\bar{\bar{\boldsymbol{\mathcal{S}}}}_{\text{upper}}$ is full-rank. To evaluate the positive definiteness of $\bar{\bar{\boldsymbol{\mathcal{S}}}}_{\text{upper}}$ we use Sylvester's criterion [65]. According to the criterion, if every leading principle minor of $\bar{\bar{\boldsymbol{\mathcal{S}}}}_{\text{upper}}$ is positive, then $\bar{\bar{\boldsymbol{\mathcal{S}}}}_{\text{upper}}$ is positive definite. The leading principle minor is defined as the determinant of the leading principle sub-matrix. The leading principle sub-matrix of order p of an $L\times L$ matrix is obtained by deleting the last $L-p$ rows and columns of the matrix. Let $\bar{\bar{\boldsymbol{\mathcal{S}}}}_{\text{upper},p}$ denote the leading principle sub-matrix of order p of $\bar{\bar{\boldsymbol{\mathcal{S}}}}_{\text{upper}}$. For $p=1$, it gives $\bar{\bar{\boldsymbol{\mathcal{S}}}}_{\text{upper},1} = 1$. For

$p > 1$, we have $\bar{\tilde{\boldsymbol{\mathcal{S}}}}_{\text{upper},p} = \left(1 - \sin(\frac{2\pi}{2^{B+1}})\right)\mathbf{I}_p + \boldsymbol{\omega}\boldsymbol{\omega}^\dagger$ with $\boldsymbol{\omega} = \sqrt{\sin(\frac{2\pi}{2^{B+1}})}\mathbf{1}$ in which the vector $\mathbf{1}$ is of size $p \times 1$ for $p = 2, \ldots, L$ where every element is equal to one. Then, we apply Sherman-Morrison formula [66] to obtain the leading principle minor of $\bar{\tilde{\boldsymbol{\mathcal{S}}}}_{\text{upper},p}$ which gives

$$\det\left(\bar{\tilde{\boldsymbol{\mathcal{S}}}}_{\text{upper},p}\right) = \left(1 + (p-1)\sin\left(\tfrac{2\pi}{2^{B+1}}\right)\right)\left(1 - \sin\left(\tfrac{2\pi}{2^{B+1}}\right)\right)^{p-1}. \tag{30}$$

Having the leading principle minors in hand, one can determine that for what symbol size L and phase-shifter resolution B the matrix $\bar{\tilde{\boldsymbol{\mathcal{S}}}}_{\text{upper}}$ (respectively, $\bar{\tilde{\boldsymbol{\mathcal{S}}}}$) is positive definite, and hence the equivalent reconfigured channel matrix is full-rank. We note that for any symbol size and phase-shifter resolution $\det\left(\bar{\tilde{\boldsymbol{\mathcal{S}}}}_{\text{upper},1}\right) = 1 > 0$. Also, for any symbol size L and phase-shifter resolution $B = 1$, (30) becomes 0 for $p = 2, \ldots, L$. That is, $\bar{\tilde{\boldsymbol{\mathcal{S}}}}_{\text{upper}}$ is not positive definite. Consequently, the equivalent reconfigured channel matrix is not full-rank. Further, for any symbol size L and phase-shifter resolution $B > 1$, (30) is always positive for $p = 2, \ldots, L$ which means all the leading principle minors are positive. Therefore, $\bar{\tilde{\boldsymbol{\mathcal{S}}}}_{\text{upper}}$ is positive definite and the equivalent reconfigured channel matrix is full-rank. Although $\bar{\tilde{\boldsymbol{\mathcal{S}}}}_{\text{upper}}$ is positive definite, for some cases, its determinant is close to zero which may result in an ill-conditioned system. For instance, when $L = 4$ and $B = 2$, $\det\left(\bar{\tilde{\boldsymbol{\mathcal{S}}}}_{\text{upper}}\right) = 0.0784$ ($\det\left(\bar{\tilde{\boldsymbol{\mathcal{S}}}}_{\text{upper}}\right) = \det\left(\bar{\tilde{\boldsymbol{\mathcal{S}}}}_{\text{upper},L}\right)$). To resolve this issue, the resolution B should be chosen properly.

Appendix C
Proof of Theorem 2

Let assume that phase-shifter resolution B is chosen that the Hermitian matrix $\tilde{\boldsymbol{\mathcal{S}}}$ defined in (24), and accordingly the normalized $\tilde{\boldsymbol{\mathcal{S}}}$, is positive definite and its inverse exists as well. Here, to derive the upper bound, we start by finding an upper bound for $(\bar{\tilde{\boldsymbol{\mathcal{S}}}}^{-1})_{\ell,\ell}$ as following. Let $\lambda_{\max}(\cdot)$ and $\lambda_{\min}(\cdot)$ denote the maximum and the minimum eigenvalues of a matrix $(\cdot)$, respectively. Since $\bar{\tilde{\boldsymbol{\mathcal{S}}}}^{-1}$ is positive definite, i.e., $\det(\bar{\tilde{\boldsymbol{\mathcal{S}}}}^{-1}) \geq C$, we have $0 < \lambda_{\min}(\bar{\tilde{\boldsymbol{\mathcal{S}}}}^{-1}) \leq (\bar{\tilde{\boldsymbol{\mathcal{S}}}}^{-1})_{\ell,\ell} \leq \lambda_{\max}(\bar{\tilde{\boldsymbol{\mathcal{S}}}}^{-1})$. So, we have

$$\begin{aligned}(\bar{\tilde{\boldsymbol{\mathcal{S}}}}^{-1})_{\ell,\ell} \leq \lambda_{\max}(\bar{\tilde{\boldsymbol{\mathcal{S}}}}^{-1}) &\overset{(a)}{=} \lambda^{-1}_{\min}(\bar{\tilde{\boldsymbol{\mathcal{S}}}}) \\ &\overset{(b)}{\leq} \frac{1}{C}\left(\frac{\sum_{\ell=2}^{L}\lambda_\ell(\bar{\tilde{\boldsymbol{\mathcal{S}}}})}{L-1}\right)^{L-1} \overset{(c)}{<} \frac{1}{C}\left(\frac{L}{L-1}\right)^{L-1}.\end{aligned} \tag{31}$$

To get (a), since $\bar{\tilde{\boldsymbol{\mathcal{S}}}}$ is a positive definite matrix, $\lambda_{\max}(\bar{\tilde{\boldsymbol{\mathcal{S}}}}^{-1}) = \lambda^{-1}_{\min}(\bar{\tilde{\boldsymbol{\mathcal{S}}}})$ holds [60]. Step (b) is explained as follows. Noting $\prod_{\ell=1}^{L}\lambda_\ell(\bar{\tilde{\boldsymbol{\mathcal{S}}}}) = \det(\bar{\tilde{\boldsymbol{\mathcal{S}}}}) \geq C$, it gives $C\lambda^{-1}_{\min}(\bar{\tilde{\boldsymbol{\mathcal{S}}}}) \leq \prod_{\ell=2}^{L}\lambda_\ell(\bar{\tilde{\boldsymbol{\mathcal{S}}}})$. Applying the arithmetic-geometric inequality to $\prod_{\ell=2}^{L}\lambda_\ell(\bar{\tilde{\boldsymbol{\mathcal{S}}}})$ results in (b). To get (c), we note that $\sum_{\ell=2}^{L}\lambda_\ell(\tilde{\boldsymbol{\mathcal{S}}}) < \sum_{\ell=1}^{L}\lambda_\ell(\tilde{\boldsymbol{\mathcal{S}}}) = \text{tr}(\tilde{\boldsymbol{\mathcal{S}}}) = L$.

Now, the received SNR of the ℓth symbol is given by

$$\rho_\ell = \frac{P_t}{N_t N_r}\frac{1}{(\tilde{\boldsymbol{\mathcal{S}}}^{-1})_{\ell,\ell}\sigma^2} > \kappa'\|\mathbf{h}_g\|^2, \tag{32}$$

in which $\kappa' = \frac{1}{C}a\rho\left(\frac{L}{L-1}\right)^{L-1}$, and a and ρ are defined in (13). Then, the SER expression is obtained as

$$\text{P}(\hat{s}_\ell \to s_\ell|\mathbf{h}_g) < \frac{M-1}{M}e^{-\kappa'\|\mathbf{h}_g\|^2}. \tag{33}$$

Following the same procedure in Theorem 1 in [60], it yields

$$\text{P}(\hat{s}_\ell \to s_\ell) = \mathbb{E}_{\mathbf{h}_g}[\text{P}(\hat{s}_\ell \to s_\ell|\mathbf{h}_g)] < \frac{M-1}{M}\kappa'^{-N_tN_r}.$$

Appendix D
Proof of Corollary 1

Recall that at each lens antenna the number of oriented beams is equal to the number of its selected TSAs. Since an independent AWGN noise is taken into account for each TSA, the noise term in (7), z_{t,n_r}, is comprised of the summation of all noise terms of those TSAs in each lens antenna, i.e., $z_{t,n_r} = \sum_{n_t=1}^{N_t} n_{t,n_r,n_t}$, where $n_{t,n_r,n_t} \sim \mathcal{CN}(0, \sigma_n^2)$. Due to the $i.i.d$ property of n_{t,n_r,n_t}, the variance of z_{t,n_r} is equal to $\sigma^2 = N_t\sigma_n^2$. Regarding (14), the SNR for the symbol s_ℓ is given by $\rho_\ell = \frac{P_t}{N_tN_r}\frac{\|\mathbf{h}_g\|^2}{\sigma^2} = \frac{P_t}{N_tN_r}\frac{\|\mathbf{h}_g\|^2}{N_t\sigma_n^2}$. Taking the average with respect to the channel vector, it yields $\rho = \frac{P_t}{N_tN_r}\frac{N_tN_r}{N_t\sigma_n^2} = \frac{P_t}{N_t\sigma_n^2}$.

Appendix E
Proof of Theorem 3

Let us start from (14) in Theorem 1. The outage probability is defined as

$$p_{\text{out}} = 1 - \text{P}\left(\rho_\ell > \gamma\right) = 1 - \text{P}\left(\|\mathbf{h}_g\|^2 > \frac{\gamma\sigma^2 N_tN_r}{P_t}\right). \tag{34}$$

In practice, finding the exact PDF of $\|\mathbf{h}_g\|^2$ is not trivial. To the best of the authors' knowledge, two different types of techniques are available to approximate the PDF of the sum of variables with log-normal distribution. The first technique assumes that the PDF of the sum of log-normal variables is log-normal [67], [68]. To systematically estimate the parameters of the log-normal distribution, i.e., μ' and η', four methods are proposed: Wilkinson [67], Schwartz-Yeh [67], Farley [67], and Cumulants matching [68]. The main advantage of these methods is to systematically estimate the parameters. Although for the outage probability less than 0.1 these methods result in high estimation error [69]. Other advantages and disadvantages of these methods are widely studied in [69]. The second technique relaxes the log-normal distribution assumption and focuses on finding accurate PDFs for a wide range of the outage probabilities. To this end, several methods such as minimax approximation [70], least square approximation [71], and log skew normal approximation [72] are proposed. Due to the complicated PDF of these methods, calculating (34) is intractable. On the other hand, the log-normal distribution assumption makes the first technique attractive to use. Hence, we adopt a log-normal PDF for the variable $\|\mathbf{h}_g\|^2$. Since the systematic methods do not provide an accurate estimation for μ' and η', we do exhaustive search to find the best value of μ' and η'. With the log-normal assumption, the PDF of

$10\log_{10}(\|\mathbf{h}_g\|^2)$ is normal with μ'-mean and η'^2-variance in dB. Hence, we have

$$p_{\text{out}} = 1 - \mathrm{P}\left(\|\mathbf{h}_g\|^2 > \frac{\gamma\sigma^2 N_t N_r}{P_t}\right) \overset{(a)}{=} 1 - \mathrm{P}\left(10\log_{10}(\|\mathbf{h}_g\|^2) > 10\log_{10}\left(\frac{\gamma\sigma^2 N_t N_r}{P_t}\right)\right) \tag{35}$$

To get (a), we apply $10\log_{10}$ to both sides and notice that the logarithm is an incremental function. Using the fact that $10\log_{10}(\|\mathbf{h}_g\|^2)$ closely has a normal distribution, (17) is obtained.

REFERENCES

[1] M. A. Almasi, H. Mehrpouyan, V. Vakilian, N. Behdad, and H. Jafarkhani, "A new reconfigurable antenna MIMO architecture for mmWave communication," *in Proc. IEEE ICC*, pp. 1–7, May 2018.

[2] T. S. Rappaport *et al.*, "Millimeter wave mobile communications for 5G cellular: It will work!" *IEEE Access*, vol. 1, pp. 335–349, May 2013.

[3] T. S. Rappaport, R. W. Heath Jr, R. C. Daniels, and J. N. Murdock, *Millimeter wave wireless communications*. Pearson Education, 2014.

[4] R. W. Heath *et al.*, "An overview of signal processing techniques for millimeter wave MIMO systems," *IEEE J. Sel. Topics Signal Process.*, vol. 10, no. 3, pp. 436–453, Apr. 2016.

[5] M. Xiao *et al.*, "Millimeter wave communications for future mobile networks," *IEEE J. Sel. Areas Commun.*, vol. 35, no. 9, pp. 1909–1935, Sept. 2017.

[6] F. Rusek, D. Persson, B. K. Lau, E. G. Larsson, T. L. Marzetta, O. Edfors, and F. Tufvesson, "Scaling up MIMO: Opportunities and challenges with very large arrays," *IEEE Signal Process. Mag.*, vol. 30, no. 1, pp. 40–60, Jan. 2013.

[7] J. Kim and I. Lee, "802.11 WLAN: history and new enabling MIMO techniques for next generation standards," *IEEE Commun. Mag.*, vol. 53, no. 3, pp. 134–140, Mar. 2015.

[8] S. Sun *et al.*, "MIMO for millimeter-wave wireless communications: beamforming, spatial multiplexing, or both?" *IEEE Commun. Mag.*, vol. 52, no. 12, pp. 110–121, Dec. 2014.

[9] L. Jiang and H. Jafarkhani, "Multi-user analog beamforming in millimeter wave MIMO systems based on path angle information," *IEEE Trans. Wireless Commun.*, vol. 18, no. 1, pp. 608–619, Jan. 2019.

[10] O. El Ayach *et al.*, "Spatially sparse precoding in millimeter wave MIMO systems," *IEEE Trans. Wireless Commun.*, vol. 13, no. 3, pp. 1499–1513, Mar. 2014.

[11] F. Sohrabi and W. Yu, "Hybrid digital and analog beamforming design for large-scale antenna arrays," *IEEE J. Sel. Topics Signal Process.*, vol. 10, no. 3, pp. 501–513, Apr. 2016.

[12] X. Gao *et al.*, "Energy-efficient hybrid analog and digital precoding for mmWave MIMO systems with large antenna arrays," *IEEE J. Sel. Areas Commun.*, vol. 34, no. 4, pp. 998–1009, Apr. 2016.

[13] S. Payami, M. Ghoraishi, and M. Dianati, "Hybrid beamforming for large antenna arrays with phase shifter selection," *IEEE Trans. Wireless Commun.*, vol. 15, no. 11, pp. 7258–7271, Nov. 2016.

[14] J. Brady, N. Behdad, and A. M. Sayeed, "Beamspace MIMO for millimeter-wave communications: System architecture, modeling, analysis, and measurements," *IEEE Trans. Antennas Propag.*, vol. 61, no. 7, pp. 3814–3827, July 2013.

[15] Y. Zeng, R. Zhang, and Z. N. Chen, "Electromagnetic lens-focusing antenna enabled massive MIMO: Performance improvement and cost reduction," *IEEE J. Sel. Areas Commun.*, vol. 32, no. 6, pp. 1194–1206, June 2014.

[16] Y. Zeng and R. Zhang, "Millimeter wave MIMO with lens antenna array: A new path division multiplexing paradigm," *IEEE Trans. Commun.*, vol. 64, no. 4, pp. 1557–1571, Apr. 2016.

[17] T. Kwon, Y.-G. Lim, B.-W. Min, and C.-B. Chae, "RF lens-embedded massive MIMO systems: Fabrication issues and codebook design," *IEEE Trans. Microw. Theory Techn.*, vol. 64, no. 7, pp. 2256–2271, July 2016.

[18] Y. Zeng and R. Zhang, "Cost-effective millimeter-wave communications with lens antenna array," *IEEE Wireless Commun.*, vol. 24, no. 4, pp. 81–87, Aug. 2017.

[19] B. He and H. Jafarkhani, "Low-complexity reconfigurable MIMO for millimeter wave communications," *IEEE Trans. Commun.*, vol. 66, no. 11, pp. 5278–5291, Nov. 2018.

[20] A. Sayeed and J. Brady, "Beamspace MIMO for high-dimensional multiuser communication at millimeter-wave frequencies," *in Proc. IEEE GLOBECOM*, pp. 3679–3684, Dec. 2013.

[21] B. Badamchi *et al.*, "Design of compact reconfigurable ultra-wideband slot antenna with switchable single/dual band notch functions," *IET Microw., Antennas & Propag.*, vol. 8, no. 8, pp. 541–548, June 2014.

[22] B. Badamchi, A. Valizade, P. Rezaei, and Z. Badamchi, "A reconfigurable square slot antenna with switchable single band, UWB and UWB with band notch function performances," *ACESJ*, vol. 29, no. 5, pp. 383–390, May 2014.

[23] P.-Y. Qin *et al.*, "Polarization reconfigurable U-slot patch antenna," *IEEE Trans. Antennas Propag.*, vol. 58, no. 10, pp. 3383–3388, July 2010.

[24] H. Yazdani and A. Vosoughi, "On the spectrum sensing, beam selection and power allocation in cognitive radio networks using reconfigurable antennas," *in Proc. IEEE CISS*, pp. 1–7, Mar. 2019.

[25] S. Shad, S. Kausar, and H. Mehrpouyan, "Waveguide-fed lens based beam-steering antenna for 5G wireless communications," *in Press IEEE APSURSI*, July 2019. [Online]. Available: https://arxiv.org/pdf/1903.11177.pdf

[26] B. A. Cetiner *et al.*, "Multifunctional reconfigurable MEMS integrated antennas for adaptive MIMO systems," *IEEE Commun. Mag.*, vol. 42, no. 12, pp. 62–70, Dec. 2004.

[27] A. Grau, H. Jafarkhani, and F. De Flaviis, "A reconfigurable multiple-input multiple-output communication system," *IEEE Trans. Wireless Commun.*, vol. 7, no. 5, pp. 1719–1733, May 2008.

[28] F. Fazel *et al.*, "Space-time-state block coded MIMO communication systems using reconfigurable antennas," *IEEE Trans. Wireless Commun.*, vol. 8, no. 12, pp. 6019–6029, Dec. 2009.

[29] V. Vakilian, J.-F. Frigon, and S. Roy, "Space-frequency block code for MIMO-OFDM communication systems with reconfigurable antennas," *in Proc. IEEE GLOBECOM*, pp. 4221–4225, Dec. 2013.

[30] J. G. Andrews *et al.*, "Modeling and analyzing millimeter wave cellular systems," *IEEE Trans. Commun.*, vol. 65, no. 1, pp. 403–430, Jan. 2017.

[31] S. Niknam and B. Natarajan, "On the regimes in millimeter wave networks: Noise-limited or interference-limited?" *in Proc. IEEE ICC Workshops*, pp. 1–6, May 2018.

[32] R. J. Weiler *et al.*, "Millimeter-wave outdoor access shadowing mitigation using beamforming arrays," *in Proc IEEE Eur. Conf. Antennas Propag.*, pp. 1–5, Apr. 2016.

[33] M. R. Akdeniz *et al.*, "Millimeter wave channel modeling and cellular capacity evaluation," *IEEE J. Sel. Areas Commun.*, vol. 32, no. 6, pp. 1164–1179, June 2014.

[34] M. Flament and M. Unbehaun, "Impact of shadow fading in a mm-wave band wireless network," *In Proc. IEEE WPMC*, pp. 427–432, Nov. 2000.

[35] J. Choi, "On the macro diversity with multiple BSs to mitigate blockage in millimeter-wave communications," *IEEE Commun. Lett.*, vol. 18, no. 9, pp. 1653–1656, Sept. 2014.

[36] A. K. Gupta, J. G. Andrews, and R. W. Heath, "Macrodiversity in cellular networks with random blockages," *IEEE Trans. Wireless Commun.*, vol. 17, no. 2, pp. 996–1010, Feb. 2018.

[37] H. Jafarkhani, *Space-Time Coding: Theory and Practice*. Cambridge University Press, 2005.

[38] R. J. Weiler, M. Peter, W. Keusgen, and M. Wisotzki, "Measuring the busy urban 60 GHz outdoor access radio channel," *In Proc. IEEE ICUWB*, pp. 166–170, Sept. 2014.

[39] V. Vakilian *et al.*, "System for resolving channel sparsity in multiple-input multiple-output systems using (re) configurable antennas, and methods of making and using the same," Oct. 3 2016, US Patent App. 15/284,123.

[40] B. Schoenlinner *et al.*, "Wide-scan spherical-lens antennas for automotive radars," *IEEE Trans. Microw. Theory Techn.*, vol. 50, no. 9, pp. 2166–2175, Sept. 2002.

[41] M. A. Almasi *et al.*, "Reconfigurable antennas in mmWave MIMO systems," *arXiv preprint arXiv:1710.05111*, 2017.

[42] ——, "Reconfigurable antenna multiple access for 5G mmWave systems," *in Proc. IEEE ICC Workshops*, pp. 1–6, May 2018.

[43] ——, "Lens-based millimeter wave reconfigurable antenna NOMA," *in Press IEEE ICC Workshops*, May 2019.

[44] M. D. Wright *et al.*, "MEMS reconfigurable broadband patch antenna for conformal applications," *IEEE Trans. Antennas Propag.*, vol. 66, no. 6, pp. 2770–2778, June 2018.

[45] A. M. Sayeed, "Deconstructing multiantenna fading channels," *IEEE Trans. Signal Process.*, vol. 50, no. 10, pp. 2563–2579, Oct. 2002.

[46] Fernandes *et al.*, "Dielectric lens antennas," *Handbook of antenna technologies*, pp. 1–54, 2014.

[47] M. A. B. Abbasi *et al.*, "Lens-based beamformer for low-complexity millimeter-wave cellular systems," *in Proc. ESA Workshop on Millimetre-Wave Techn. and Applications*, pp. 1–4, Oct. 2018.

[48] Z. Gua, X. Wang, and W. Heng, "Millimeter-Wave channel estimation based on 2-D beamspace MUSIC method," *IEEE Trans. Wireless Commun.*, vol. 16, no. 8, pp. 5384 – 5394, Aug. 2017.

[49] S. Hur *et al.*, "Millimeter wave beamforming for wireless backhaul and access in small cell networks," *IEEE Trans. Commun.*, vol. 61, no. 10, pp. 4391–4403, Oct. 2013.

[50] A. Alkhateeb, O. El Ayach, G. Leus, and R. W. Heath, "Channel estimation and hybrid precoding for millimeter wave cellular systems," *IEEE J. Sel. Topics Signal Process.*, vol. 8, no. 5, pp. 831–846, Oct. 2014.

[51] M. A. Almasi, R. Amiri, and H. Mehrpouyan, "A new millimeter wave MIMO system for 5G networks," *arXiv preprint arXiv:1807.04851*, 2018.

[52] F. Hansen and F. I. Meno, "Mobile fading—Rayleigh and lognormal superimposed," *IEEE Trans. Veh. Technol.*, vol. 26, no. 4, pp. 332–335, Nov. 1977.

[53] A. Abdi and M. Kaveh, "K distribution: an appropriate substitute for Rayleigh-lognormal distribution in fading-shadowing wireless channels," *Electron. Lett.*, vol. 34, no. 9, pp. 851–852, Apr. 1998.

[54] U. Karabulut *et al.*, "Spatial and temporal channel characteristics of 5G 3D channel model with beamforming for user mobility investigations," *IEEE Commun. Mag.*, vol. 56, no. 12, pp. 38–45, Dec. 2018.

[55] M. K. Simon and M.-S. Alouini, *Digital communication over fading channels*. John Wiley & Sons, 2005.

[56] S. Bryan *et al.*, "A compact filter-bank waveguide spectrometer for millimeter wavelengths," *IEEE Trans. THz Sci. Technol.*, vol. 5, no. 4, pp. 598–604, July 2015.

[57] V. Tarokh, H. Jafarkhani, and A. R. Calderbank, "Space-time block codes from orthogonal designs," *IEEE Trans. Inf. Theory*, vol. 45, no. 5, pp. 1456–1467, July 1999.

[58] S. M. Alamouti, "A simple transmit diversity technique for wireless communications," *IEEE J. Sel. Areas Commun.*, vol. 16, no. 8, pp. 1451–1458, Oct. 1998.

[59] H. Jafarkhani, "A quasi-orthogonal space-time block code," *IEEE Trans. Commun.*, vol. 49, no. 1, pp. 1–4, Jan. 2001.

[60] Y. Shang and X.-G. Xia, "Space–time block codes achieving full diversity with linear receivers," *IEEE Trans. Inf. Theory*, vol. 54, no. 10, pp. 4528–4547, Oct. 2008.

[61] F. Bohagen, P. Orten, and G. E. Oien, "Design of optimal high-rank line-of-sight MIMO channels," *IEEE Trans. Wireless Commun.*, vol. 6, no. 4, pp. 1420–1425, Apr. 2007.

[62] S. L. H. Nguyen *et al.*, "On the mutual orthogonality of millimeter-Wave massive MIMO channels," *in Proc. IEEE 81st Vehicular Technology Conference (VTC Spring)*, pp. 1–5, May 2015.

[63] M. K. Murugan and S. S. Adams, "Hurwitz-Radon inspired maximal three-dimensional real orthogonal designs," *Australasian Journal of Combinatorics*, vol. 54, pp. 151–162, Oct. 2012.

[64] G. H. Golub and C. F. Van Loan, *Matrix computations*. JHU press, 2012.

[65] R. A. Horn and C. R. Johnson, *Matrix analysis*. Cambridge university press, 2012.

[66] D. A. Harville, *Matrix algebra from a statistician's perspective*. Taylor & Francis Group, 1998.

[67] S. C. Schwartz and Y. S. Yeh, "On the distribution function and moments of power sums with log-normal components," *Bell Syst. Tech. J.*, vol. 61, no. 7, pp. 1441–1462, Sept. 1982.

[68] D. Schleher, "Generalized Gram-Charlier series with application to the sum of log-normal variates (corresp.)," *IEEE Trans. Inf. Theory*, vol. 23, no. 2, pp. 275–280, Mar. 1977.

[69] N. C. Beaulieu, A. A. Abu-Dayya, and P. J. McLane, "Comparison of methods of computing lognormal sum distributions and outages for digital wireless applications," *in Proc. IEEE ICC*, pp. 1270–1275 vol.3, May 1994.

[70] N. C. Beaulieu and Qiong Xie, "Minimax approximation to lognormal sum distributions," *in Proc. IEEE VTC*, vol. 2, pp. 1061–1065 vol.2, Apr. 2003.

[71] L. Zhao and J. Ding, "Least squares approximations to lognormal sum distributions," *IEEE Trans. Veh. Technol.*, vol. 56, no. 2, pp. 991–997, Mar. 2007.

[72] X. Li, Z. Wu, V. D. Chakravarthy, and Z. Wu, "A low-complexity approximation to lognormal sum distributions via transformed log skew normal distribution," *IEEE Trans. Veh. Technol.*, vol. 60, no. 8, pp. 4040–4045, Oct. 2011.

Mojtaba Ahmadi Almasi received the B.Sc. degree in electrical engineering from Urmia University, Urmia, West Azerbaijan, Iran, in 2010 and the M.S. degree in electrical engineering from Iran University of Science and Technology, Tehran, Iran, in 2012. He is currently working toward the Ph.D. degree in electrical engineering at Boise State University, ID, USA. His current research interests are wireless communications and signal processing with emphasis on mmWave communications. He has received the IEEE Conference on Communication (ICC) best paper award from the Communication Theory Symposium in 2018.

Roohollah Amiri (S'18) received his B.Sc. and M.Sc. degrees (Hons.) in communication systems from the Iran University of Science and Technology (IUST), in 2011 and 2013, respectively. Since 2016, he is pursuing a Ph.D. degree with the Department of Electrical and Computer Engineering, Boise State University. From June 2019 to February 2020 he was a visiting scholar at the Wireless Networking and Communications Group (WNCG) at the University of Texas at Austin. His research interests include wireless communications and networking, machine learning, self-organizing networks, millimeter-wave communications, and resource allocation. He has actively served as a reviewer for the IEEE Transactions and the flagship conferences, such as the ICC and the GLOBECOM.

Hamid Jafarkhani is a Chancellor's Professor at the Department of Electrical Engineering and Computer Science, University of California, Irvine, where he is also the Co-Director of the Networked Systems Program, the Director of Center for Pervasive Communications and Computing and the Conexant-Broadcom Endowed Chair. He was a Visiting Scholar at Harvard University in 2015 and a Visiting Professor at California Institute of Technology in 2018. Among his awards are the IEEE Marconi Prize Paper Award in Wireless Communications, the IEEE Communications Society Award for Advances in Communication, and the IEEE Eric E. Sumner Award.

Dr. Jafarkhani is listed as an ISI highly cited researcher. According to the Thomson Scientific, he is one of the top 10 most-cited researchers in the field of "computer science" during 1997-2007. He is the 2017 Innovation Hall of Fame Inductee at the University of Maryland's School of Engineering. He is a Fellow of AAAS, an IEEE Fellow, and the author of the book "Space-Time Coding: Theory and Practice."

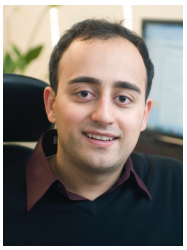

Hani Mehrpouyan (S'05-M'10) received the B.Sc. honours degree from Simon Fraser University, Burnaby, Canada in 2004 and the Ph.D. degree from Queens University, Kingston, Canada, in Electrical Engineering in 2010. From Sep.2011 to Mar. of 2012 he was a Post-Doc at Chalmers University of Technology where he led the MIMO aspects of the microwave backhauling for next generation wireless networks project. He was an Assistant Professor at California State University, Bakersfield from 2012-2015. Since 2015 he has been with Boise State University, where he now holds the position of Associate Professor. Dr. Mehrpouyan has received the IEEE Conference on Communication (ICC) best paper award from the Communication Theory Symposium. He also currently hold the position of associated editor for IEEE Communication Letters.